JGR Space Physics

RESEARCH ARTICLE
10.1029/2021JA029509

Salient Midlatitude Ionosphere-Thermosphere Disturbances Associated With SAPS During a Minor but Geo-Effective Storm at Deep Solar Minimum

Ercha Aa[1], Shun-Rong Zhang[1], Philip J. Erickson[1], Anthea J. Coster[1], Larisa P. Goncharenko[1], Roger H. Varney[2], and Richard Eastes[3]

[1]Haystack Observatory, Massachusetts Institute of Technology, Westford, MA, USA, [2]Center for Geospace Studies, SRI International, Menlo Park, CA, USA, [3]Laboratory for Atmospheric and Space Physics, University of Colorado Boulder, Boulder, CO, USA

Key Points:

- A minor but geo-effective storm at deep solar minimum produced intense subauroral polarization stream (SAPS), considerable Storm-enhanced density structure, and subauroral large-scale traveling ionospheric disturbances
- Strong westward wind enhancement of 230 m/s and large poleward wind surge of 85 m/s occurred in the post-SAPS interval
- Midlatitude total electron content and O/N_2 simultaneously showed large storm-time dynamic features, with a prolonged enhancement followed by a large reduction

Correspondence to:
E. Aa,
aercha@mit.edu

Citation:
Aa, E., Zhang, S.-R., Erickson, P. J., Coster, A. J., Goncharenko, L. P., Varney, R. H., & Eastes, R. (2021). Salient midlatitude ionosphere-thermosphere disturbances associated with SAPS during a minor but geo-effective storm at deep solar minimum. *Journal of Geophysical Research: Space Physics*, *126*, e2021JA029509. https://doi.org/10.1029/2021JA029509

Received 30 APR 2021
Accepted 15 JUN 2021

Abstract This work conducts a focused study of subauroral ion-neutral coupling processes and midlatitude ionospheric/thermospheric responses in North America during a minor but quite geo-effective storm on September 27–28, 2019 under deep solar minimum conditions. Several prominent storm-time disturbances and associated electrodynamics/dynamics were identified and comprehensively analyzed using Millstone Hill and Poker Flat incoherent scatter radar measurements, Fabry-Perot interferometer data, total electron content data from Global Navigation Satellite System observations, and thermospheric composition O/N_2 data from the Global-scale Observations of Limb and Disk mission. Despite solar minimum conditions, this minor storm produced several prominent dynamic features, in particular (a) Intense subauroral polarization stream (SAPS) of 1,000 m/s, overlapping with a deepened main trough structure. (b) An enhanced westward wind of 230 m/s and a significant poleward wind surge of 85 m/s occurred in the post-SAPS period. (c) Large-scale traveling ionospheric disturbances (TIDs) were generated and propagated equatorward across mid-latitudes in the storm main phase. TID characteristics were significantly affected by SAPS, evolving into divergent propagation patterns. (d) SAPS was situated on the poleward edge of a considerable storm-enhanced density structure. (e) The midlatitude ionosphere and thermosphere exhibited a prolonged positive storm effect in the main phase and beginning of recovery phase, with 5–10 TECU increase and 10%–30% O/N_2 enhancement for 12 h. This was followed by a considerable negative storm effect with 5–10 TECU and 20%–40% O/N_2 decrease. Results show that minor storm intervals can produce substantial mid-latitude ionospheric and thermospheric dynamics in low solar flux conditions.

1. Introduction

During a geomagnetic storm, intense injection of solar wind-magnetospheric energy and momentum into the coupled ionosphere-thermosphere (I-T) system occurs through enhanced electric fields, currents, and particle precipitation. These enhanced inputs are known to cause significant perturbations in the coupled I-T system (Buonsanto, 1999). In particular, dramatic and complicated local/global changes may occur in the I-T system in response to various chemical, dynamic, and electrodynamics driving processes, such as Joule heating, ion-drag forcing, and penetration electric field (Mendillo, 2006; Richmond & Lu, 2000). Moreover, besides the traditional concentration in storm effects within auroral/polar and equatorial regions, the midlatitude and subauroral ionosphere also experiences substantial dynamic structuring and increase in variability. These midlatitude I-T effects have been the subject of many recent community studies especially in the past decade as the observed response can exhibit far more storm-time dynamics than would be otherwise anticipated (e.g., Ferdousi et al., 2019; Raeder et al., 2016; Zhang et al., 2015). Furthermore, steep electron density gradients therein can pose detrimental effects on modern navigation and communication systems (e.g., Coster & Foster, 2007; Doherty et al., 2004). For these reasons, characterizing the storm-time midlatitude ionosphere and thermosphere perturbations and understanding the intrinsic mechanisms in triggering those perturbations are of considerable importance in frontier space weather research.

Generally, midlatitude ionosphere-thermosphere responses to a geomagnetic storm are primarily determined by various ion-neutral coupling mechanisms and relevant electrodynamic processes. These include (a) Momentum transfer via ion drag: Strong ion convection in the storm-time auroral/subauroral region can

act as a driver to accelerate neutrals, resulting in large modifications to the horizontal thermospheric neutral wind pattern (Killeen & Roble, 1984; Rishbeth, 1979). Conversely, the neutral circulation that is set up by the above-mentioned ion drag can also influence the ionosphere to drive Hall and field-aligned currents when the magnetospheric electric field is suddenly inhibited, in a configuration known as the "flywheel" effect (Deng et al., 1993; Lyons et al., 1985). (b) Energy transfer via heating: Electromagnetic energy from the magnetosphere can be transferred to the ionospheric plasma and further dissipate into the thermosphere via ion-neutral coupling in the form of Joule heating. This process further modifies the global neutral circulation and thermospheric composition (Schunk & Nagy, 2000). Moreover, at subauroral latitudes, the subauroral polarization stream (SAPS, Foster & Burke, 2002) will cause enhanced ion-neutral frictional heating and lead to considerable ion upflow associated with thermal expansion (Erickson et al., 2010; Yeh & Foster, 1990; Zhang, Erickson, et al., 2017). (c) Neutral dynamics and composition effects: Pressure gradients due to the intense Joule and particle heating in the high-latitude ionosphere will cause atmospheric upwelling and equatorward neutral wind surge, leading to both ionospheric disturbance dynamo (Blanc & Richmond, 1980) and possible thermospheric composition (e.g., O/N_2) changes (Fuller-Rowell et al., 1994). The direct effects of neutral wind through ion transport along field lines, as well as indirect effects through composition variation and the generation of dynamo electric fields, significantly impact the ionosphere. These underlying processes generate significant regional/global increases (positive storm) or decreases (negative storm) in total electron content (TEC) and electron density (e.g., Lu et al., 2014). (d) Prompt penetration electric field (PPEF) and disturbance dynamo electric field (DDEF): In response to storm-induced variations in the solar wind-magnetosphere dynamo, there is a time-delayed development of the Region-2 field-aligned current system with respect to the Region-1 field-aligned current. This delay leads to the build-up of an undershielding (overshielding) PPEF during suddenly enhanced (decreased) magnetospheric convection electric field conditions (Huang et al., 2010; Kikuchi et al., 1978; Klimenko & Klimenko, 2012; Lu et al., 2012). For the DDEF, the above-mentioned equatorward neutral wind surge can subsequently drive a westward wind component due to the Coriolis force, generating a disturbed zonal electric field in the mid- and low-latitude ionosphere via dynamo process (Blanc & Richmond, 1980; Maruyama et al., 2005). When all these factors are combined, the combination of electric fields, neutral winds, and thermospheric composition changes will generate complicated ionospheric and thermospheric variations during a storm.

In parallel with studies of these dynamic effects, continued community interest over the last several decades has focused on specifying the mechanisms and drivers behind storm-time midlatitude ionosphere and thermosphere dynamic features. Prominent drivers and associated characteristics are still a matter of study but include: (a) The subauroral polarization stream (SAPS, Foster & Burke 2002), which refers to intense westward plasma flows (a few hundred m/s) driven by large poleward electric fields in the subauroral ionosphere equatorward of the auroral precipitation zone (Erickson et al., 2011; Foster & Vo, 2002). SAPS is a broad term that can under certain circumstances be associated with embedded phenomena, such as latitudinally narrow and intense flow channel known as subauroral ion drifts (SAID) (Anderson et al., 1991; Spiro et al., 1979), or polarization jets (Galperin et al., 1974). (b) Storm-enhanced density (SED, Foster 1993), which describes a significant storm-time electron density or TEC enhancement in the local afternoon ionosphere at mid- and subauroral latitudes (Mendillo, 2006). SED structures sometimes extend to higher latitudes along a sunward/poleward elongated ridge and form a plume, which can occasionally convect into the cusp region and then into the polar cap (Foster et al., 2005). (c) Storm-induced traveling ionospheric/atmospheric disturbances (TIDs/TADs). Storm-time energy deposition in the auroral and subauroral regions can generate large amplitude atmospheric gravity waves (AGWs), which manifest in the ionosphere as large-scale TIDs (Hunsucker, 1982). These underlying processes are of great importance in transporting high-latitude energy and momentum deposition into higher altitudes and lower latitudes (Richmond, 1978). (d) Negative and positive ionospheric storm effects, with main drivers being electric fields, thermospheric neutral winds, and composition changes. As partially described above, a negative ionospheric storm is primarily caused by a decrease in O/N_2 density ratio due to thermospheric composition changes (Fuller-Rowell et al., 1994). In contrast, explaining the positive ionospheric storm remains a difficult issue since it involves many complicated and competing drivers, such as PPEF (Kikuchi et al., 1978) effects, DDEF (Blanc & Richmond, 1980) effects, as well as forcing from equatorward thermospheric neutral winds and TAD/TIDs (Balan et al., 2010).

Recently, our understanding of storm-time midlatitude ion-neutral coupling and electrodynamic processes has greatly advanced through community-wide investigation on I-T responses to a few intense geomagnetic storms, especially in the maximum and declining phase of the Solar Cycle 24. These events include but not limited to the St. Patrick's Day storms during March 17–18, 2013 and 2015 (e.g., Astafyeva et al., 2015; Huang et al., 2016; Huba et al., 2017; Nava et al., 2016; Yue et al., 2016; Zakharenkova et al., 2016; Zhong et al., 2016; Zhang, Erickson, et al., 2017; Zhang, Zhang, et al., 2017), June 22–23, 2015 storm (e.g., Astafyeva et al., 2017; Singh & Sripathi, 2017), Memorial Day storm on May 27–28, 2017 (e.g., Jonah et al., 2018; Liu et al., 2019), September 07–08, 2017 storm (e.g., Aa et al., 2019; Jimoh et al., 2019; Lei et al., 2018; Zhang et al., 2019), as well as the August 25–26, 2018 storm (Astafyeva et al., 2020). Although significant progress has been made through prior studies on these intense storms, the spatial/temporal evolution of the I-T system in each storm can be quite different and often lacks a unified explanation of the various responses. Moreover, even a seemingly modest storm around a deep solar minimum period can be highly geo-effective in causing severe observed disturbances in the I-T system (Watari, 2017). Of these features, midlatitude ion-neutral coupling processes and their physical drivers are still in need of coordinated, multi-sensor studies through observational campaigns for modest storms to allow comparison with responses seen in intense storms near solar maximum. Such studies of modest storm response provide key information for a more complete understanding of storm-time I-T response.

In this study, we investigate a minor but very geo-effective geomagnetic storm that occurred on September 27–28, 2019 in the deep minimum of solar cycle 24. The regional subauroral/midlatitude ionosphere and thermosphere responses, such as plasma drift, neutral wind, and electron density, were measured by a coordinated observational campaign within the North American longitude sector at subauroral latitudes near Millstone Hill (42.8°N, 71.5°W, MLAT: 52°). We comprehensively analyze I-T responses during this period to study several SAPS-related ion-neutral coupling processes. Ionospheric and thermospheric direct observations employed in this study include Millstone Hill incoherent scatter radar measurements and Fabry-Perot Interferometer (FPI) measurements. In addition, the storm-TEC from global navigation satellite system (GNSS) measurements and thermospheric O/N_2 density ratio data derived from Global-scale Observations of Limb and Disk (GOLD) measurements over the American sector will also be collectively investigated to understand the ionospheric storm effect and its underlying drivers. Moreover, measurements from the high-latitude Poker Flat incoherent scatter radar (PFISR) will also be used to extend and corroborate the above-mentioned results.

As a general statement, the appearance of several significant I-T disturbances in a minor storm near the solar minimum is quite unusual. In particular, the September 27–28, 2019 storm triggered a series of bright features, including intense SAPS flow, a considerable SED, strong zonal and meridional neutral wind perturbation, subauroral TIDs/TADs, and complicated positive and negative storm effects. Despite the relatively minor storm conditions, many of these features became comparable to those reported in earlier studies of severe geospace storms. These features included large SAPS and SED (Foster et al., 2007; Zou et al., 2013), strong neutral wind disturbances in zonal and particularly in meridional components (Zhang et al., 2015), as well as significant TIDs/TADs in the subauroral latitudes (Guo et al., 2018; Zhang et al., 2019). In general, therefore, a straightforward connection to severe system forcing is not possible for this minor storm, and physical processes responsible for these features thus remain highly debatable. In aggregate, these factors motivated this study as a unique opportunity to advance the current understanding of storm-time electrodynamics and neutral dynamics at mid-latitudes.

2. Data and Instrumentation

2.1. Millstone Hill Incoherent Scatter Radar

The Millstone Hill incoherent scatter radar system uses the Thomson or incoherent scatter remote ionospheric sensing technique (Evans, 1969), considered one of the most powerful ground-based methods for ionospheric dynamic observations. Millstone Hill has provided extensive and valuable auroral, subauroral, and mid-latitude observations in the North American sector (e.g., Buonsanto et al., 1992; Foster et al., 2005). The radar system uses a 2.5-MW transmitter in combination with multiple large antennas and highly sensitive radio receivers to measure ionospheric plasma state parameters (e.g., temperature, density, composition, and velocity) with full altitude profiles between 100 and 1,000 km (Foster & Vo, 2002; Erickson

et al., 2011). The Millstone Hill incoherent scatter radar system is equipped with a 46 m diameter full steerable MISA antenna and a 68 m diameter fixed zenith antenna. The MISA steerable antenna has an extensive field-of-view, which was configured in the observations reported in this study to conduct a wide-range azimuth scan from +20° to −100° at a fixed elevation of ∼6°, spanning over 30° in latitude and more than 4 h in local time at F-layer (Aa, Erickson, et al., 2020). On a near-simultaneous basis, the system's zenith antenna provided local altitude profiles in both E and F regions. For more details about Millstone Hill incoherent scatter radar data processing procedures, readers may refer to Zhang, Erickson, et al. (2017).

2.2. Fabry-Perot Interferometer

The ground-based Fabry-Perot interferometer at Millstone Hill measures thermospheric horizontal winds at an altitude of ∼250 km. Observations are based on Doppler shifts in the upper atmosphere 630.0 nm nightglow emission occurring due to dissociative recombination of O_2^+ (Zhang et al., 2015).

2.3. GNSS TEC

GNSS TEC data are generated at the Massachusetts Institute of Technology's Haystack Observatory through a processing algorithm employing 6,000+ worldwide GNSS receivers. Resulting gridded TEC products are distributed through the Madrigal data system with a spatial resolution of 1° (longitude) × 1° (latitude) and a temporal cadence of 5 min (Rideout & Coster, 2006; Vierinen et al., 2016). Besides absolute TEC, in this study, we also examined detrended TEC (dTEC) to analyze both large-scale ionospheric variation and wave-like traveling ionospheric disturbances associated with storm-time electrodynamics and dynamics. dTEC is calculated by filtering out the background TEC trend derived from a Savitzky-Golay low-pass filter method, employing a convolution process with the least-square fitting of successive subsets of TEC data points of given window size (30 min in this study) (Savitzky & Golay, 1964; Zhang et al., 2019). A threshold of 15° elevation cutoff is implemented to remove satellite-receiver ray paths close to the horizon.

2.4. GOLD O/N_2 Data

The GOLD instrument includes two identical far-ultraviolet (FUV) imaging spectrometers operating at a geostationary orbit over the longitude of 47.5°W. GOLD FUV observations image Earth's ionosphere and thermosphere by measuring airglow emissions (∼132–162 nm) at different cadences from the daytime disk, limb, occultation, and nighttime disk (Eastes et al., 2019; McClintock et al., 2020). The GOLD measurements are equivalent approximately to a constant pressure surface in the lower thermosphere (Eastes et al., 2020). This study uses the O/N_2 column-integrated density ratio derived from daytime disk imaging of OI 135.6 nm and the N_2 Lyman-Birge-Hopfield (LBH) emission measurement. The O/N_2 ratio is a proxy of thermospheric composition change and a key component in the analysis of storm-time variation in the I-T system.

2.5. The Poker Flat Incoherent Scatter Radar (PFISR)

PFISR is an incoherent scatter radar situated in Alaska at the Poker Flat Research Range (65.13°N, 147.47°W), at a location approximately corresponding to a magnetic L-shell coordinate of ∼5. The boresight of the PFISR antenna is tilted to the geomagnetic north with an elevation angle of 74° and an azimuth angle of 15° (Semeter et al., 2009; Varney et al., 2009). PFISR is a phased array radar that can transmit and receive on multiple frequency channels near 450 MHz and rapid pulse-to-pulse steering. This allows for almost simultaneous observations in various directions.

2.6. Other Observations

Besides the above-mentioned datasets, the Defense Meteorological Satellite Program (DMSP) F18 satellite cross-track plasma drift measurements will also be used. The DMSP F18 satellite flies in a sun-synchronous

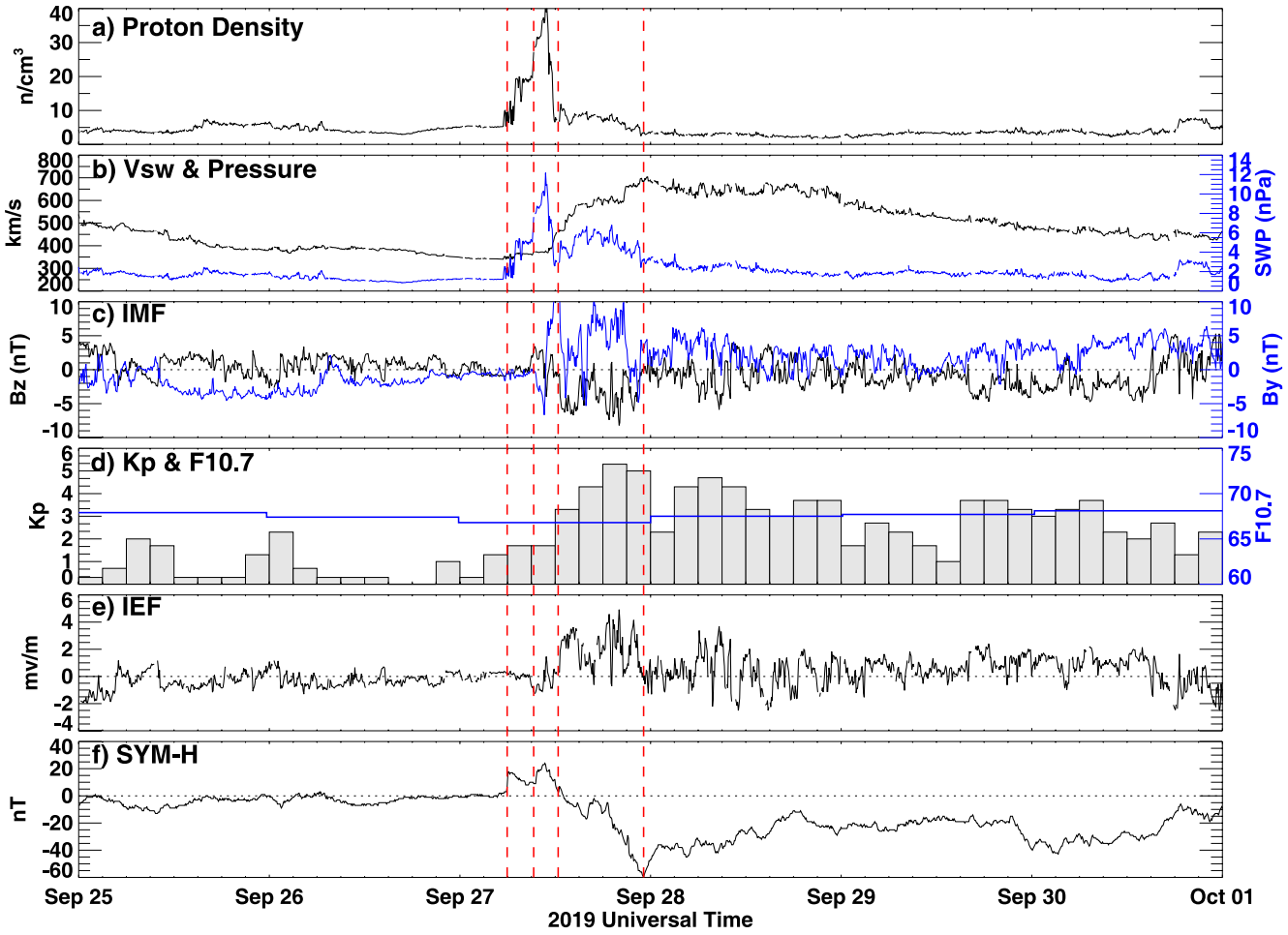

Figure 1. Temporal variation of (a) Solar wind proton density, (b) Solar wind speed and dynamic pressure, (c) Interplanetary magnetic field (IMF) By and Bz, (d) Kp and F10.7 index, (e) Interplanetary electric field (IEF), and (f) Longitudinally symmetric index (SYM-H) during September 25–October 01, 2019. Four vertical red dashed lines show the starting time of the sudden impulse (~6 UT), initial phase (~9 UT), main phase (~12.3 UT), and recovery phase (~23 UT) of the storm occurring on September 27, respectively.

polar orbit approximately along the dusk-dawn meridian at an altitude of ~840 km. Cross-track plasma drift was measured by the Special Sensor-Ions, Electrons, and Scintillation instrument onboard DMSP. A description of this data set can be found in Hairston et al. (2016) and references therein.

3. Interplanetary and Geomagnetic Conditions of September 25–30, 2019

Figure 1 shows the temporal variation of solar wind proton density, solar wind speed and dynamic pressure, interplanetary magnetic field (IMF) By and Bz components, Kp and F10.7 index, interplanetary electric field, as well as the longitudinally symmetric index (SYM-H) from September 25 to October 01, 2019. Solar activity was at a very low level during this period, with F10.7 ranging from 66 to 68 SFU (1 SFU = 10^{-22} W/m^2/Hz). Both solar wind plasma density and dynamic pressure exhibit sudden enhancements during 06–12 UT on September 27 that precede the velocity increase. This is a noticeable signature of stream interactions producing compressed plasma in the leading edge of the stream, due to the influence of a recurrent positive polarity coronal hole high-speed stream. The solar wind speed showed considerable enhancement after 12 UT on September 27 from ~350 to ~700 km/s. IMF Bz exhibited intermittent fluctuations with two considerable southward excursions on September 27. Specifically, Bz first became slightly negative at ~12 UT and remained southward for about 2–3 h before temporarily returning to zero. Later, IMF Bz exhibited a moderate southward excursion again, reaching a minimum value of −8.2 nT at 20:00 UT. At the same time as the IMF Bz southward excursion, IMF By turned from negative to positive. A modest geomagnetic

storm subsequently occurred due to the above-mentioned solar wind and IMF conditions. A sudden storm impulse was registered in the symmetric H-component (SYM-H) index at ~6 UT on September 27, followed by the compression of the magnetosphere that marked the starting of the initial phase at ~9 UT. After the beginning of the main phase at ~12:20 UT, the SYM-H index gradually became more negative during main storm phase, reaching a minimum value of −60 nT at 23:05 UT on September 27. Also, the Kp index reached 5+ during 18–24 UT on September 27. Taken as a whole, these parameters would nominally lead to a classification of this disturbance as a minor geomagnetic storm around the deep minimum of solar cycle 24, based on National Oceanic and Atmospheric Administration space weather scales (https://www.swpc.noaa.gov/noaa-scales-explanation). This classification implies a corresponding expectation of limited ionosphere and thermosphere response. However, as will be seen in the following sections, this storm was actually a highly geo-effective one that triggered a series of noticeable I-T disturbances and responses, especially in the American sector. The results of this study suggest that Dst and Kp may not always be sufficient proxies to characterize a storm's I-T effects, and additional conditions need to be considered.

4. Results

Results and discussion of storm-time I-T responses during the minor storm event in this study are elaborated in this section in the following order: (a) SAPS in the North American sector measured by the Millstone Hill incoherent scatter radar and DMSP satellites. (b) Zonal and meridional thermosphere neutral wind perturbations measured by FPI. (c) Subauroral TIDs in the vicinity of Millstone Hill. (d) SED measured by Millstone Hill and Poker Flat incoherent scatter radars. (f) Storm-time variation of midlatitude ionospheric TEC and thermospheric O/N_2 over the North American sector.

4.1. Storm-Time SAPS

As briefly mentioned above, SAPS refers to intense westward plasma flows (typically greater than several hundred m/s) driven by a strong magnetically poleward electric field in the subauroral ionosphere (Erickson et al., 2011; Foster & Burke, 2002). Figure 2a shows the Northern Hemisphere polar view of TEC distribution at 21:30 UT on the storm day in the coordinates of magnetic local time (MLT) and geomagnetic latitude (MLAT), superposing DMSP F18 satellite cross-track ion velocity along its approximate dusk-dawn orbital path during 21:20–21:43 UT. There were two noticeable westward flow peaks around 60°–68° MLAT in the dusk sector. SAPS was identified as the local peak westward flow at ~60° MLAT with a magnitude of ~1,000 m/s, while the ion convection returning flow is seen as the other poleward peak separated by around 5°. Moreover, SAPS was also collocated with moderately reduced background TEC (i.e., in/near the main ionospheric trough) when compared with its equatorward edge. The TEC reduction may have resulted from an enhanced recombination rate associated with increased ion-neutral frictional heating due to large SAPS flows therein (Schunk, 1975), as well as SAPS-related large horizontal flux gradients.

Figure 2b shows line-of-sight Millstone Hill ISR plasma velocities for a full azimuth scan with 6° elevation together with the TEC map at 22:30 UT. SAPS flow signatures were clearly identified as the enhanced westward plasma flow of ~1,000 m/s at around 60°–62° MLAT and 16–17 MLT, which is consistent with the result of DMSP cross-track velocity.

To better present ion convection and SAPS flow in the subauroral region to the northwest of Millstone Hill's location, we used line-of-sight plasma velocity west-looking data from the wide-coverage azimuth scan to the northwest of Millstone Hill between −70° and −10° azimuth angle and between 300 and 450 km in altitude, with the mean geodetic location at ~(51°N, 87°W). We then computed the magnetic eastward plasma drift component perpendicular to the magnetic field V_{perE} using a flow angle correction factor that assumes SAPS flow is aligned along constant magnetic latitude contours. This is a valid assumption near the base of SED as in this observational case and as introduced in several prior studies (Aa, Erickson, et al., 2020; Erickson et al., 2011; Zhang, Erickson, et al., 2017). In a similar manner, we also calculated the magnetic northward component of plasma drift perpendicular to the magnetic field V_{perN}). Specifically, V_{perN} was calculated from a poleward-looking subset of the line of sight velocity data where the observing direction was approximately perpendicular to the field line near the magnetic meridian at the F region with the mean location at ~(52°N, 75°W). These settings and analysis methods allow for sensitive determination of V_{perE}

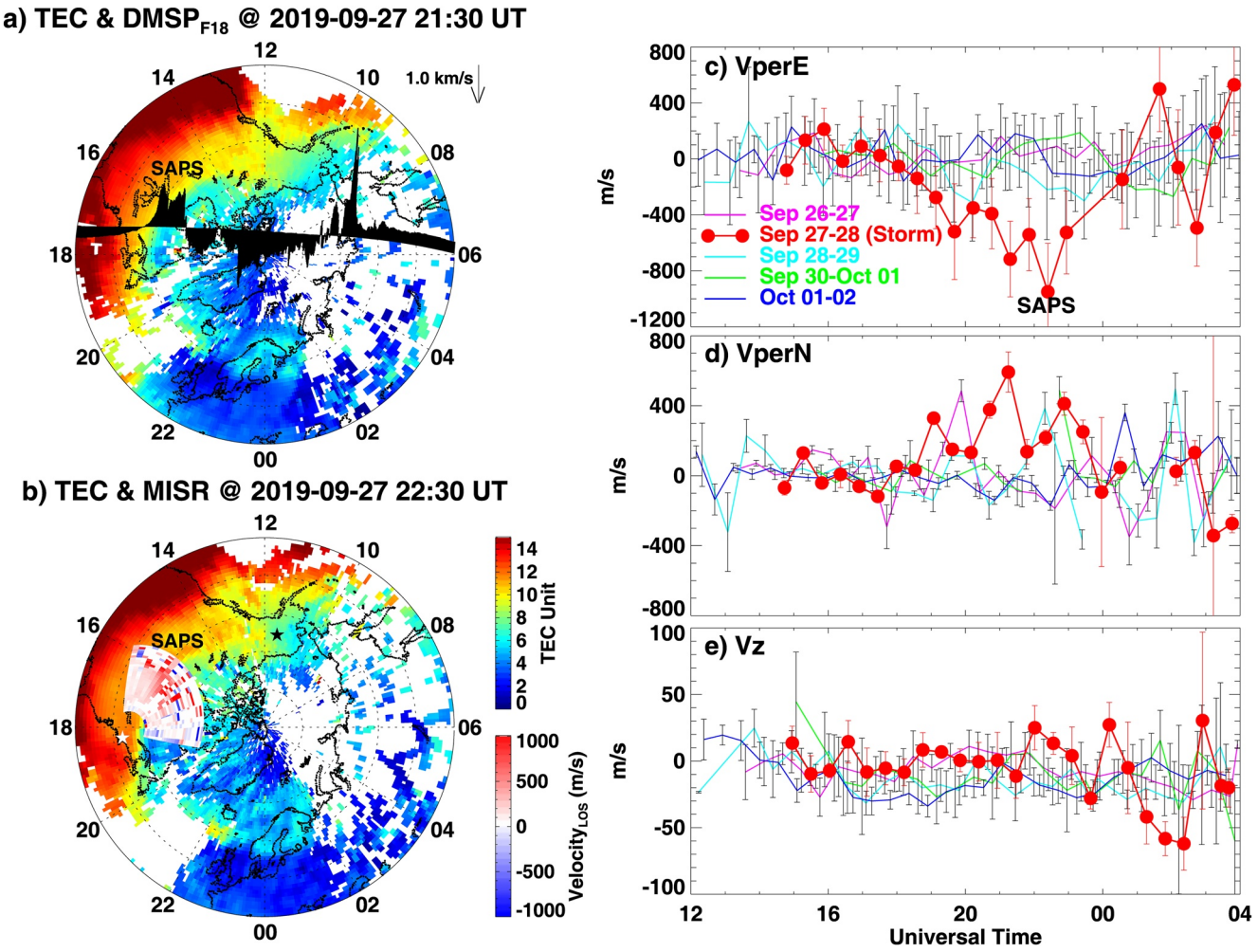

Figure 2. (a) and (b) Northern Hemisphere polar view of total electron content at 21:30 UT and 22:30 UT on September 27, 2019 in the coordinates of magnetic local time and geomagnetic latitude. Overlapping plots show (a) Defense Meteorological Satellite Program F18 cross-track ion velocities in the dawn-dusk plane during 21:20–21:43 UT and (b) Line-of-sight plasma velocities for a full azimuth scan of Millstone Hill (white star) incoherent scatter radar during 22:15–22:31 UT. Concentric dashed circles are plotted in 10° interval with outermost one representing 40° MLAT. PFISR location is also marked by a black star. (c) and (d) V_{perE} (perpendicular eastward) and V_{perN} (perpendicular northward) plasma convection speed in the F-region estimated from the radar's wide-coverage low-elevation experiment during five consecutive experiment days (see text). (e) Vertical ion drifts between 300 and 350 km at Millstone Hill derived from ISR zenith antenna measurements.

and V_{perN} vectors in the ionospheric F region with reliable accuracy and small uncertainty. For more details about the plasma velocity vector calculation, readers may refer to Zhang, Erickson, et al. (2017).

Using the above-mentioned methods and low-elevation Millstone Hill azimuth scans, Figures 2c and 2d show the temporal variation of the derived averaged eastward and northward plasma flow in the F region for each scan during five consecutive experiments days for this storm event. Results clearly show that the zonal ion velocity V_{perE} exhibited a significant westward drift reaching a maximum speed of ~1,000 m/s at 22:30 UT on September 27. This drift was statistically significant and well beyond the uncertainty envelope calculated from other non-storm days during 20–24 UT. The enhanced plasma westward drift, together with the intense line-of-sight ion flow and DMSP cross-track drift in the North American subauroral area, clearly indicates the existence of strong SAPS and convection flow near the low-density main trough region to the northwest of Millstone Hill. These high-speed ion flows could influence local heating and cause thermospheric disturbances as will be discussed later.

Figure 2d shows that V_{perN} also exhibited daytime enhancements that were very evident between 19 and 23 UT (14–18 LT) on September 27, in configurations which are signatures of intermittent enhancements

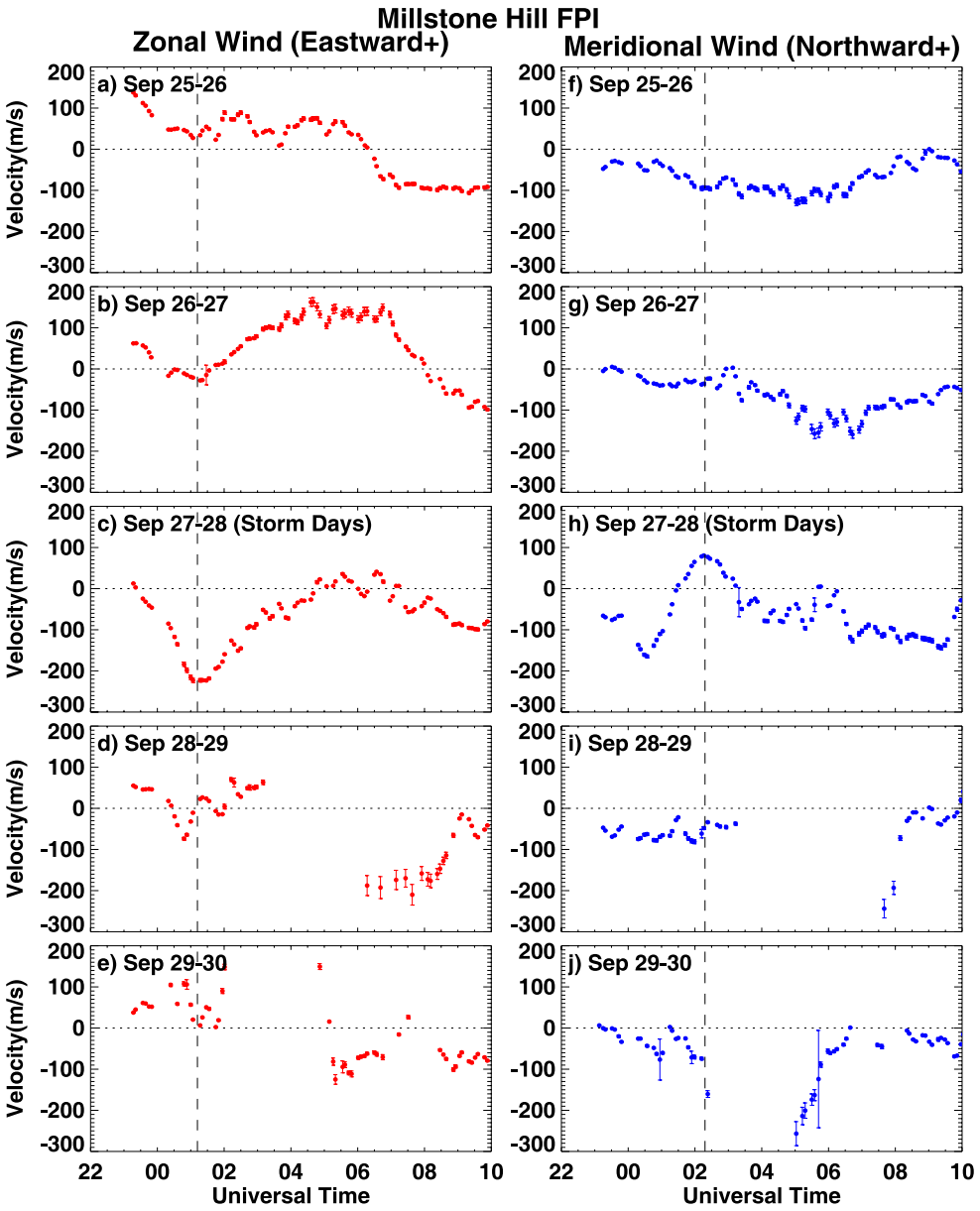

Figure 3. Millstone Hill FPI 630 nm (red-line) measurements of thermospheric neutral wind and corresponding uncertainties for zonal (a)–(e) and meridional (f)–(j) components during September 25–30, 2019. Vertical dashed lines mark the approximate time of intense westward and poleward wind surge during storm days shown in Figures 3c and 3h, respectively.

of penetration electric fields. In addition, Figure 2e displays the temporal variation of vertical ion drift between 300 and 350 km at Millstone Hill derived from zenith antenna measurements. We note that vertical drifts showed a large negative diversion at 01–03 UT on September 28, reaching a peak amplitude of around −60 m/s. This phenomenon occurred at 3–4 h delay behind local SAPS and could be related to zonal electric field response and/or meridional wind disturbances potentially associated with SAPS flows. We will further discuss this mechanism in the next subsection.

4.2. SAPS-Related Thermospheric Wind Response

Figure 3 presents Millstone Hill FPI nighttime measurements of zonal and meridional thermospheric neutral winds during September 25–30, 2019. Results, particularly in Figure 3c, indicate that during the

storm main phase (September 27–28), the zonal wind began to exhibit a noticeable westward diversion from ~23 UT and remained strongly westward for the next 3–4 h, reaching a maximum amplitude of ~230 m/s around 01 UT. This feature did not occur on other non-storm days, and the storm time westward wind disturbance gradually diminished around 04–05 UT close to local midnight.

Figures 3f–3j display the temporal variation of the meridional wind. During the storm time shown in Figure 3h, the meridional wind component exhibited both strong equatorward and poleward surges in the local premidnight sector. Specifically, a considerable equatorward wind surge occurred after 00 UT on September 28. This equatorward wind surge is an expected storm-time dynamic characteristic primarily driven by increased Joule heating and thermosphere expansion at high latitudes (Fuller-Rowell et al., 1994; Rishbeth, 1998). The equatorward wind surge reached a maximum magnitude of ~170 m/s at 0030–0100 UT on September 28 (~20 LT). This value is considerably larger than non-storm days since the storm-time wind surge was added to the background day-to-night neutral circulation pattern and was reinforced by the enhanced antisunward flow associated with expanded convection pattern (Buonsanto, 1999).

However, the equatorward neutral wind response to storm conditions also changed drastically poleward at 0130 UT and remained in this direction for about 2 h before returning equatorward. The maximum amplitude of this poleward wind surge was 85 m/s at 0200–0230 UT, with a time delay of 1.5–2 h following the peak westward wind and 3.5–4 h following SAPS peak value. Despite minor storm forcing, these intense poleward wind surges and time-dependent responses are quite similar to that of the St. Patrick's day storm in 2015 as shown by Zhang et al. (2015) and Guo et al. (2018) and will be further analyzed in the Section 5.

Beyond thermospheric effects, ionospheric effects of this poleward wind surge through ion-neutral coupling were manifested in vertical ion drifts shown in Figure 2e. As mentioned in the previous subsection, during intervals between 01 and 03 UT on September 28 with strong poleward wind, the vertical ion drift also exhibited a larger-than-average downward flow compared to reference days, while the zonal electric fields were quite small as inferred from both Figures 1d and 2d. This suggests that the neutral drag force associated with the enhanced poleward wind may have played an important role in causing enhanced downward ion drifts. Such effects are fully consistent with observations from the St Patrick's day storm results presented in (Zhang, Erickson, et al., 2017) and provide a clear illustration that even a minor storm can trigger very similar I-T coupling features to that seen in severe storms.

4.3. SAPS-Related TIDs

Many prior storm-time TID studies have focused on the generation and propagation of large-scale TIDs (LSTIDs) primarily excited by high-latitude energy deposition due to enhanced Joule and particle heating (e.g., Ding et al., 2007; Jonah et al., 2018; Zakharenkova et al., 2016). In contrast, only a few studies in the literature have discussed the potential influence of SAPS on TID dynamics at subauroral latitudes (e.g., Guo et al., 2018; Zhang et al., 2019). Thus, in the current study, we will place emphasis on subauroral TIDs and further investigate their possible correlation with the existence of SAPS. Figure 4 shows two detrended TEC keograms as a function of latitude at 75°–85°W and longitude at 45°–50°N in the North American sector from 18 UT on September 27 to 04 UT on September 28. Significant wave-like TID structures can be clearly seen in those two panels. However, the TID structures exhibited quite different patterns in the pre-SAPS and post-SAPS intervals.

First, equatorward propagating LSTIDs was the predominant pattern in the pre-SAPS interval between 19 and 22 UT. As the solar wind speed reached 600+ km/s at around 15:00 UT, and Kp index reached 5+ at 18:00 UT, well-organized LSTIDs feature due to auroral-zone energy ingestion started to show since ~19:00 UT. In the top panel of Figure 4, at least four continuous large-scale wavefronts can be recognized. These LSTIDs propagated equatorward from auroral zone all the way to low-latitude region with an estimated period of ~40–50 min, horizontal velocity of ~800 m/s, and wavelength of 2,000–2,500 km. In the bottom panel, the corresponding LSTID wavefronts can be identified that aligned approximately along a zonal direction, spanning more than 60° in longitude from the United States west coast to east coast. These typical features and parameters values are consistent with prior storm-time LSTIDs studies (e.g., Jonah et al., 2018; Shiokawa et al., 2002; Zakharenkova et al., 2016).

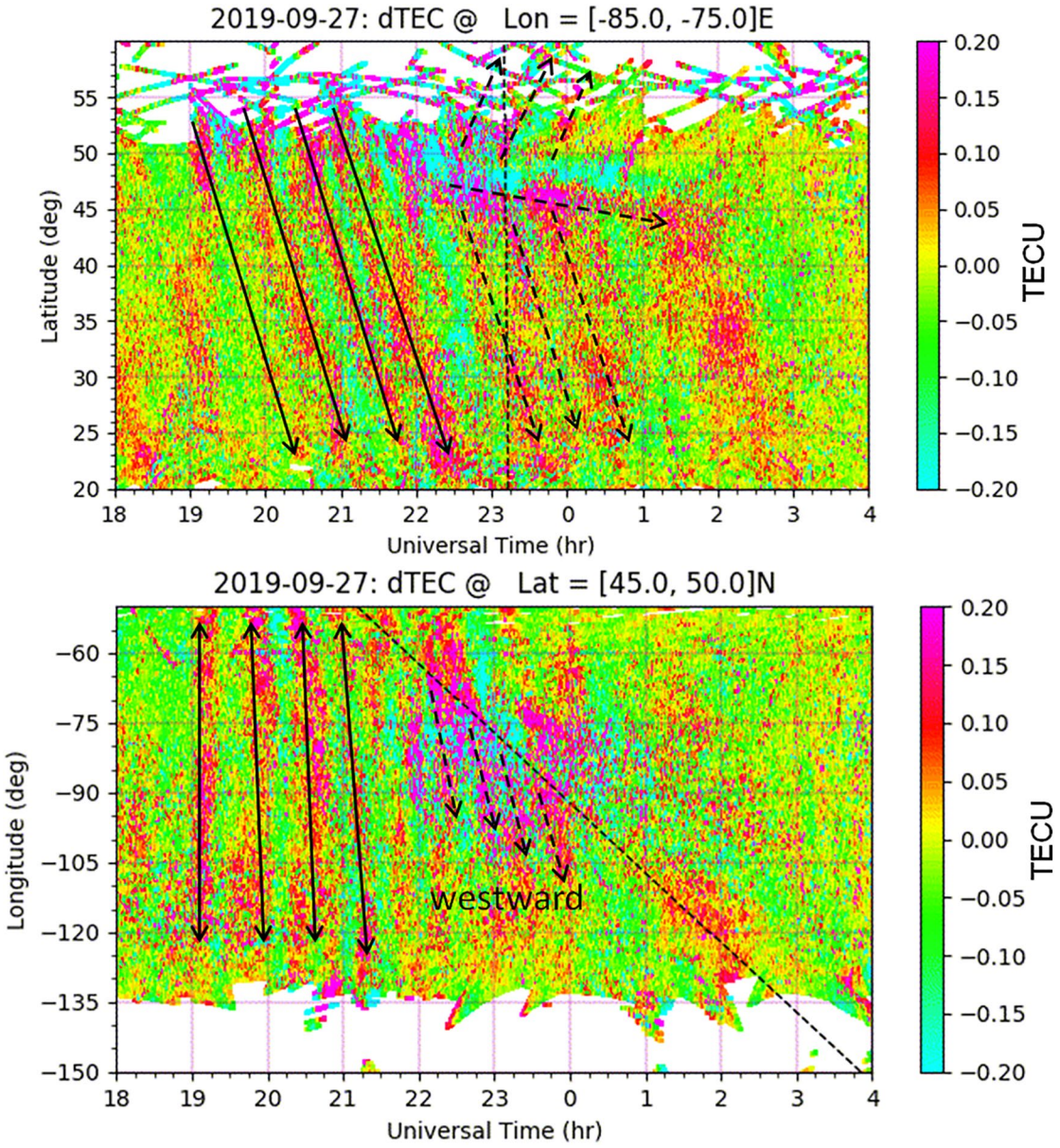

Figure 4. Temporal variation of the detrended total electron content keogram as a function of (top) latitude at 75°–85°W and (bottom) longitude at 45°–50°N in the North American sector on September 27–28, 2019. The dashed line represents the local sunset terminator. The solid lines with (top) arrows and (bottom) double-arrows mark equatorward propagating large-scale traveling ionospheric disturbances and their corresponding zonal wave fronts, respectively. The dashed lines with arrows mark the adjusted traveling ionospheric disturbances propagation pattern near dusk at times following the appearance of subauroral polarization stream.

However, the previous LSTIDs pattern went through a considerable adjustment between 22 and 00 UT around the dusk sector: the TID source region appeared to shift from the auroral zone to the subauroral region. Recall from Figure 2c that intense SAPS of ~1,000 m/s occurred between 22 and 00 UT to the northwest of Millstone Hill. The top panel of Figure 4 also showed that divergent TID formats with both equatorward and some hint of poleward propagating components were generated in the subauroral region of 45°–50°N following the appearance of the SAPS channel. This might suggest that the SAPS-related strong ion flow and frictional heating could effectively drive or adjust the TID pattern and caused the observed divergent propagating pattern. This phenomenon is similar to those indicated in Zhang et al. (2019) and will be further analyzed in the discussion section. Furthermore, the TID wavefronts also exhibited additional quasi-zonal propagating components of perturbation to the equatorward edge of the SAPS region. In

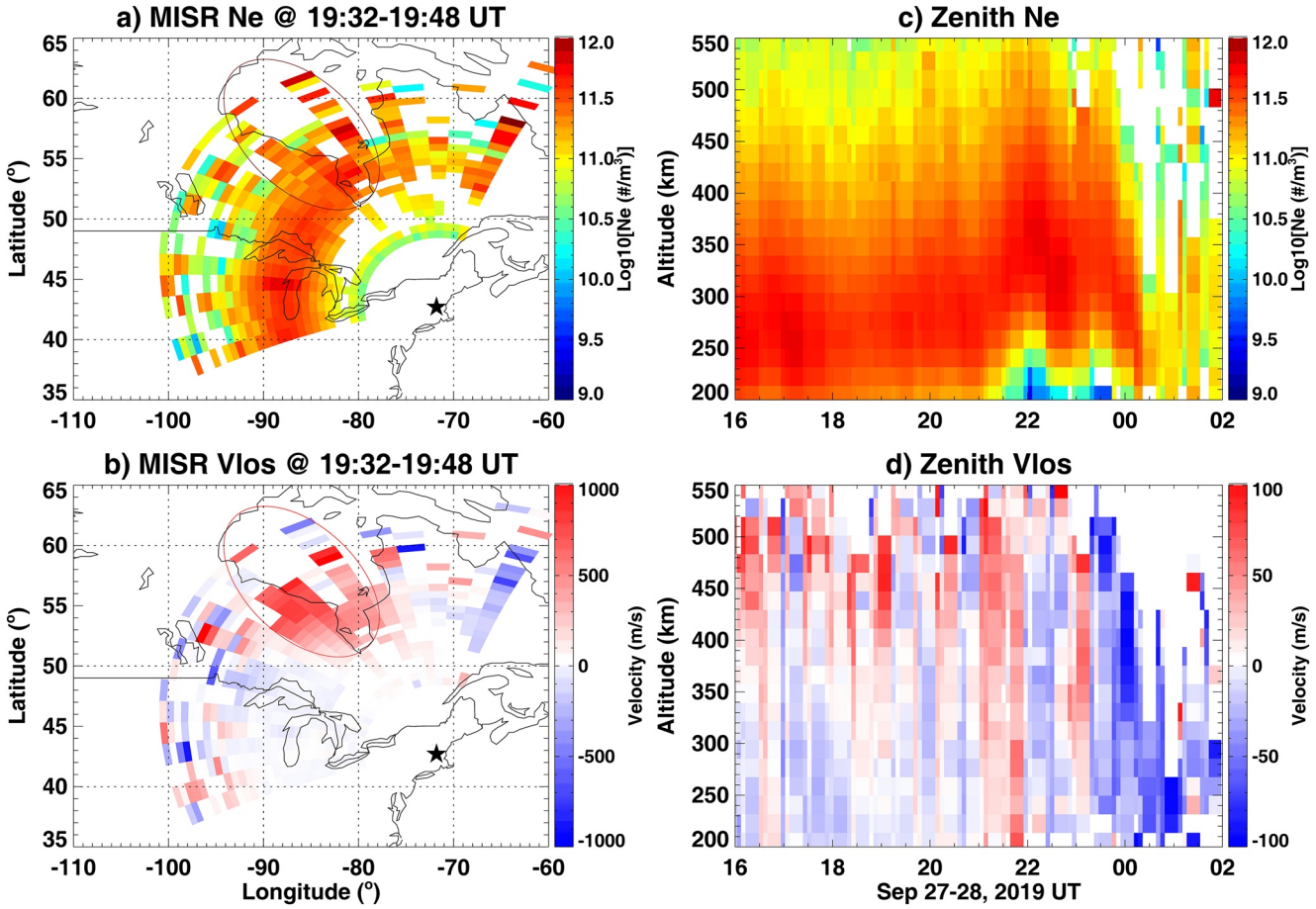

Figure 5. (a) and (b) Millstone Hill ISR (star) wide-coverage results of electron density and line-of-sight plasma velocities for a full azimuth scan during 19:32–19:48 UT on September 27. The red ellipse represents the signatures of storm-enhanced density. (c) and (d) Electron density and vertical plasma velocity as a function of altitude and universal time measured by zenith antenna of Millstone Hill incoherent scatter radar.

particular, in the bottom panel of Figure 4, the previous double-arrow wavefronts started to rotate and break, exhibiting a clear westward propagating trend following the occurrence of SAPS as shown by the dashed arrows with an estimated velocity of ~600–800 m/s. This enhanced zonal perturbation with fast-moving features indicates that SAPS-related strong westward plasma flow might have generated the increased westward propagating components of LSTIDs.

4.4. SAPS-Related SED

A clear SED feature in the North American sector was also observed by the Millstone Hill ISR in this minor but quite geo-effective storm. Specifically, Figure 5a shows *Ne* measurements for a full low-elevation azimuth scan of Millstone Hill ISR. A clear SED signature can be seen as a plume-like *Ne* elongation structure in the North American sector, marked with a red ellipse, starting from the location slightly north of the Great Lakes and extending westward/poleward in the afternoon sector. In addition, Figure 5b displays plasma line-of-sight velocity from Millstone Hill's field of view. A significant stream-like sunward/poleward plasma flow of ~600–800 m/s in the F region can be seen approximately collocated with SED in the afternoon sector. This signature of enhanced *Ne* that associated with large sunward/poleward plasma flow is consistent with previous SED studies (Foster et al., 2007; Zou et al., 2013).

Moreover, SED and SAPS effects also appeared in zenith/vertical observations at Millstone Hill. In particular, Figures 5c and 5d show the temporal-altitudinal variation of *Ne* and vertical plasma velocity measured by zenith antenna. It can be seen that a strong upward ion drift of ~50–100 m/s appeared around 21–22 UT

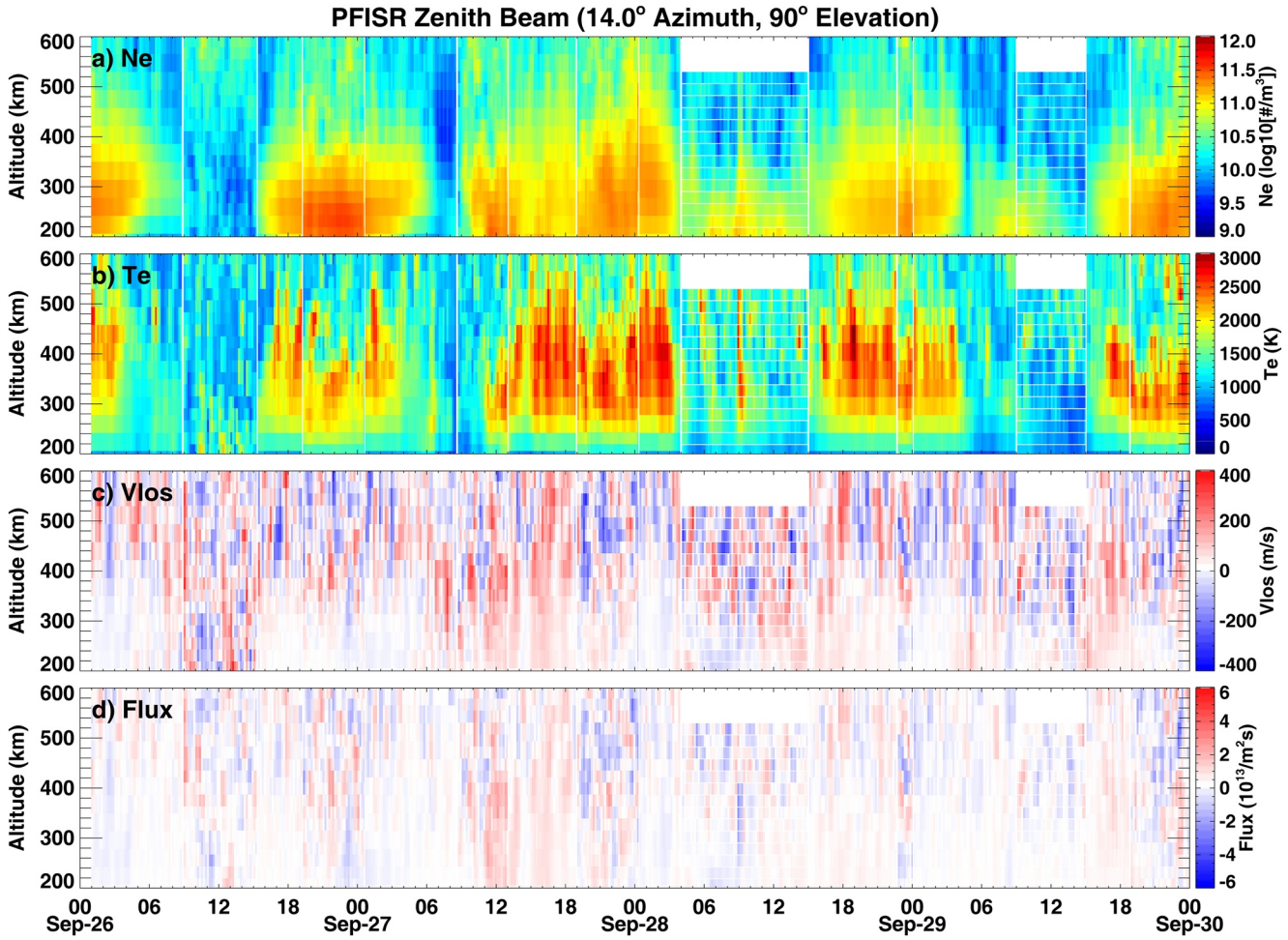

Figure 6. Poker Flat incoherent scatter radar zenith beam observations in the long-pulse mode during September 26–30, 2019. (a)–(d) Altitudinal profiles of electron density (*Ne*), electron temperature (*Te*), line-of-sight velocity, and ion flux (i.e., the product of *Ne* and line-of-sight Velocity).

across the whole F region and topside ionosphere. This phenomenon of ion upflow in the midst of SAPS interval could be driven by enhanced frictional heating and associated expansion in the SAPS region, plus some contribution from penetration electric fields after IMF Bz turning southward. This ion upflow was followed by an electron density enhancement at 350 km and higher altitude due to the reduced recombination rate caused by the F-layer uplift in the topside ionosphere. The above-mentioned phenomenon is a marker of the local passage of SED over the Millstone Hill. Furthermore, the plasma velocity exhibited a large downward flow between 23 and 01 UT, possibly due to neutral drag effects from the poleward wind surge, as has been shown in Figures 2 and 3.

In this study, we also briefly examined PFISR observations to broaden and corroborate the storm-time ion-neutral coupling processes that were mentioned above, especially SED and SAPS-related effects. During this storm period, PFISR was operated in three different modes: an International Polar year mode, a MSWINDs mode, as well as a world day 35 mode. There were four beams with common directions among those modes. Beam 1 was the zenith beam pointing to the magnetic north. Beam 2 was the southward beam that approximately pointed in the anti-parallel direction along the local magnetic field line. Beams 3 and 4 were pointing northwest and northeast, respectively. For more details on beam configurations, readers may refer to Zou et al. (2013). Figure 6 shows the altitudinal variation of zenith beam observations during September 26–30, 2019. Between 23 UT on September 27 and 03 UT on September 28 among storm main phase, there was a modest electron density enhancement among 350–500 km comparing with the previous quiet day, and the corresponding hmF2 was slightly elevated around 50–100 km. These were local SED

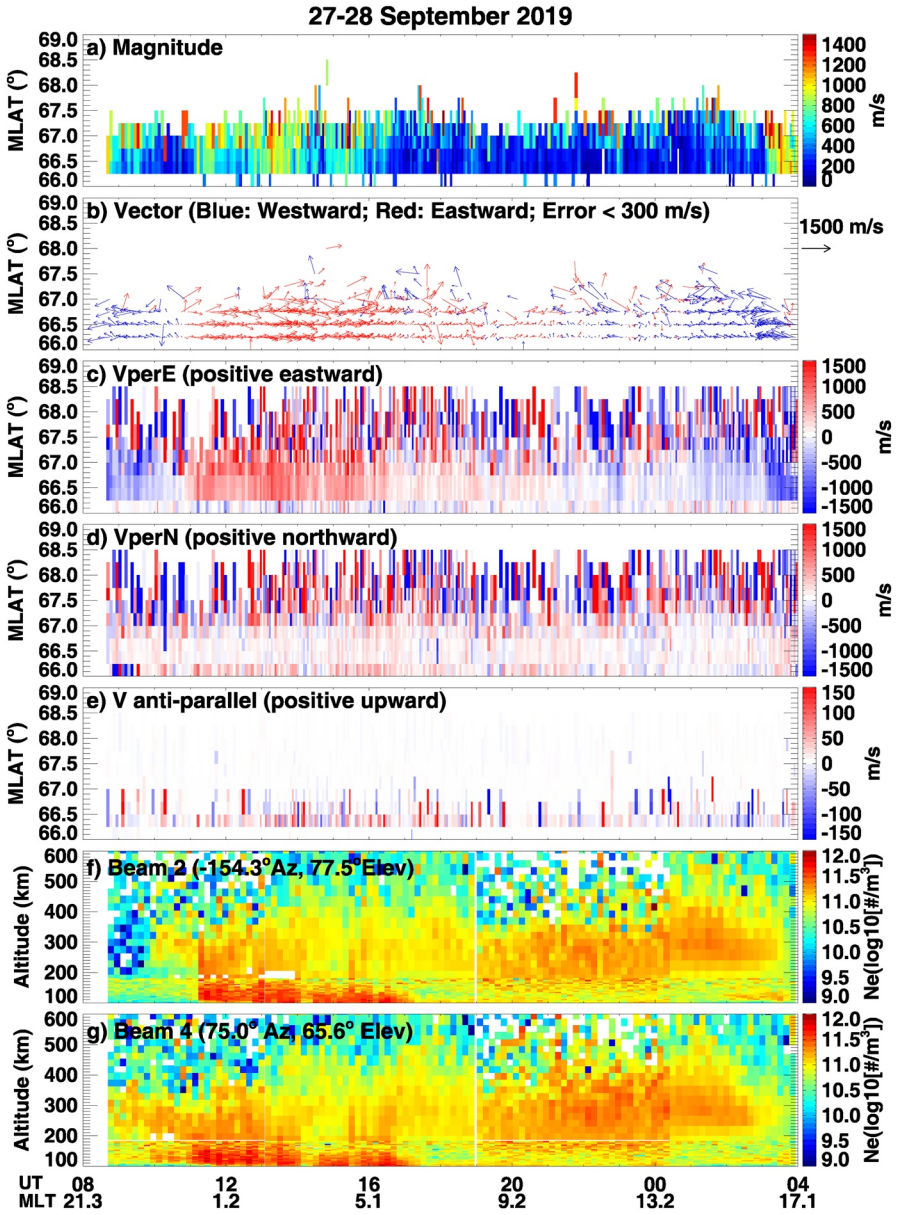

Figure 7. Poker Flat incoherent scatter radar observations between 08 UT on September 27 and 04 UT on September 28. (a) and (b) The E × B convection flow magnitude and vector. (c)–(e) V_{perE} (perpendicular eastward), V_{perN} (perpendicular northward), and anti-parallel plasma flow speed along the filed line in the F-region. (f) and (g) Altitudinal profile of *Ne* for beam 2 and beam 4, respectively. *Ne* below 180 km is from the alternating code pulse measurement, while that above 180 km is from the long pulse measurement.

features near PFISR that related to the SAPS/SED signature in TEC maps shown in Figure 2b. Moreover, the corresponding electron temperature within the interval of 23–03 UT also exhibited moderate enhancement of a few hundred K as compared to quiet time values. This enhanced electron temperature could partially come from the contribution of soft electron precipitation, which produces ionization in the F region and topside ionosphere as shown by previous modeling and observational studies (e.g., Millward et al., 1999; Su et al., 1999; Zou et al., 2017).

To provide a more comprehensive analysis of the storm-time ionospheric convection near Poker Flat, Figures 7a–7e shows the reconstructed vector velocity product from all PFISR beams between 08 UT on September 27 and 04 UT on September 28. These results include the E × B convection flow magnitude, vector

distribution, V_{perE}, V_{perN}, and anti-parallel plasma flow velocity as a function of UT and geomagnetic latitude. The convection flow at PFISR remained weak before 11 UT. With the passing of the stream interaction region and the beginning of the main phase, the convection pattern quickly expanded into the PFISR field-of-view, as showed by the large increase of convection flow speed between 12 and 17 UT in Figures 7a–7d. In comparison, PFISR zenith beam result (Figure 6c) also showed enhanced plasma vertical flow (>200 m/s) during 12–17 UT predominantly due to the contribution from the E × B convection flow. In addition, during 22–02 UT, the altitudinal profile observations from Beam 2 (Figure 7f) and Beam 4 (Figure 7g) showed slightly elevated hmF2 and enhanced *Ne*. These phenomena were associated with northwestward plasma flow on the order of several hundreds of m/s around 22:50 UT as shown in Figures 7b–7d, which is consistent with the DMSP and Millstone Hill ISR measurements as shown in Figure 2. Zou et al. (2013) and Zou et al. (2014) indicated that these northwestward **E** × **B** flows collocated with SED can be either SAPS or enhanced convection flows. These played an important role for the density increase around PFISR due to their projected components in the vertical direction, which lifted plasma up to regions with lower recombination rate. Later, a much larger westward velocity enhancement was registered at 02–04 UT, which is very similar to other past PFISR dusk-side SAPS observations (e.g., Lyons et al., 2015).

4.5. Positive and Negative Ionosphere/Thermosphere Storm Effects

We next investigate the storm-time variation of GNSS TEC and GOLD O/N_2 data to further analyze electrodynamic and thermospheric effects. To better understand storm-time variation, we removed the averaged TEC and O/N_2 reference values of seven quiet-time (all 3-h $Kp \leq 2+$) days prior to the storm: September 19–23 and 25–26. We note that there was a minor Antarctic sudden stratosphere warming (SSW) event that occurred from late August to mid-September in 2019, which caused ionospheric TEC anomalies at low latitudes and in the southern hemisphere (Goncharenko et al., 2020). Given this factor, to minimize the effects on our study of SSW-related driving forces from the lower atmosphere, we will focus on discussing the mid-latitude ionosphere and thermosphere response only in the North American sector, and limit selection of reference days as indicated above.

Figure 8 shows ΔTEC and $\Delta O/N_2$ maps from GOLD observations in the American-Atlantic sector between 09 and 21 UT with a 3-h interval on September 27 and 28, respectively. Note that GOLD O/N_2 data is only available during the daytime. For the midlatitude ionosphere over the North American region, TEC value showed a noticeable enhancement of 5–10 TECU between 15 and 21 UT on September 27 within the main phase of the storm, yet later showed a considerable reduction of 5–10 TECU between 12–21 UT on September 28 in the recovery phase. Similarly, the midlatitude O/N_2 ratio also showed a modest increase of 10%–20% on September 27 and a significant decrease of 20%–40% on September 28.

To better display storm-time ionosphere/thermosphere variation and to make a comparison with the above-mentioned Millstone Hill ISR/FPI campaign results, Figures 9a–9d show the latitudinal-temporal variation of the absolute TEC, ΔTEC, O/N_2, and $\Delta O/N_2$ values during September 26–28 centered on 75°W, close to the Millstone Hill longitude in the North American sector. Note the mid-latitude ionospheric TEC and thermospheric O/N_2 exhibited a long-duration positive storm effect for more than 12 h during the main phase on September 27, and TEC showed a persistent enhancement during local nighttime on September 28 in the recovery phase. However, the subsequent variation of mid-latitude TEC and O/N_2 showed a strong negative storm effect on the local daytime of September 28. We will further analyze these opposite storm effects as well as associated ionosphere-thermosphere processes.

Considerable positive deviation of ionospheric TEC from the reference values was observed since ~13 UT on September 27 shortly after the beginning of the main phase. In the meantime, the IMF Bz exhibited a modest southward excursion, followed by some large fluctuations between negative and zero before reaching a minimum value of −8.2 nT at ~20 UT. Between 14 and 21 UT, the low-latitude TEC around the northern crest of the equatorial ionization anomaly (EIA) showed a large daytime increase of 10–15 TECU. Correspondingly, the mid-latitude ionospheric TEC between 20 and 50°N also exhibited a considerable daytime increase of 5–10 TECU during the storm main phase, which continued for at least 12 h before gradually subsided in the nighttime. Similarly, the mid-latitude O/N_2 value showed a simultaneous 10%–20% enhancement throughout the daytime following the onset of the storm. Besides the electrodynamic effect of penetration electric field, this long-lived and synchronous mid-latitude positive I-T storm effect could also

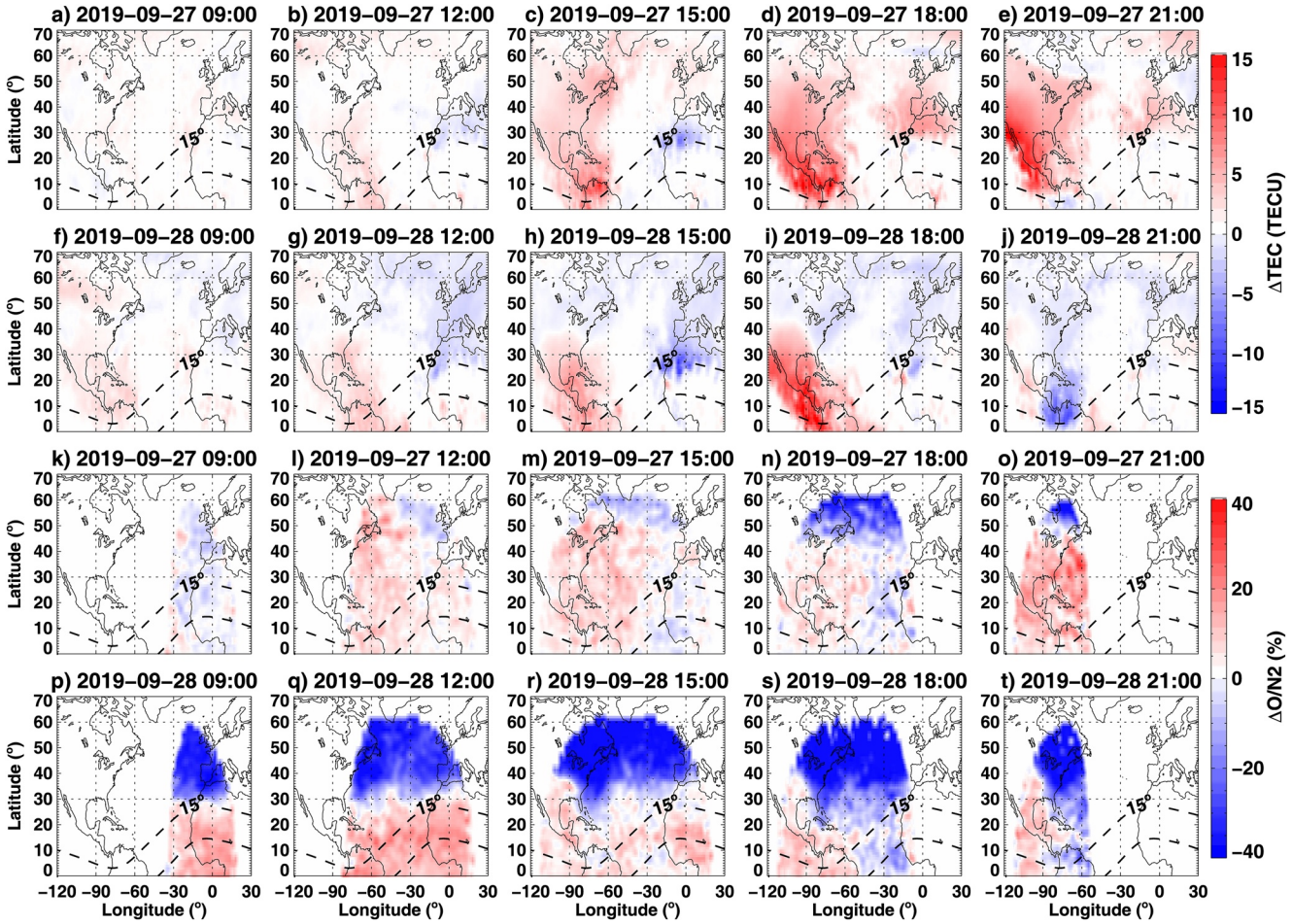

Figure 8. (a)–(j) ΔTEC and (k–t) $\Delta O/N_2$ variation in the Northern American-Atlantic sector between 09–21 UT with 3-h interval on September 27 and 28, respectively. The geomagnetic equator and 15° line were marked by dashed lines.

be ascribed to two other possible mechanisms: (a) Downwelling of neutral atomic oxygen caused by storm-time thermospheric circulation (Fuller-Rowell et al., 1994; Rishbeth, 1998): The upwelling and divergence of the polar atmosphere heating caused O/N_2 decrease in high latitudes. In contrast, the altered thermospheric circulation leads to convergence and downwelling of the neutral species through constant pressure level at low and mid-latitudes, increasing atomic O density relative to molecular constituents and thereby causing the TEC/*Ne* enhancement (Buonsanto, 1999; Burns et al., 1995; Crowley & Meier, 2008; Ngwira et al., 2012). (b) TEC enhancement caused by F-layer uplifting due to equatorward neutral wind surge (e.g., Burns et al., 1991; Mendillo, 2006; Immel et al., 2001): An equatorward neutral wind surge at mid-latitudes is a common storm-time feature of the thermosphere (Lu et al., 2008; Mendillo, 2006). Recall from Figure 3 that strong equatorward neutral wind occurred near Millstone Hill around 23-01 UT on September 27–28 before its poleward reversal. Moreover, the detrended TEC results in Figure 4 showed noticeable large-scale TID structures starting at 18 UT. The presence of equatorward neutral wind surge is consistent with the presence of these large-scale TIDs. All this information collectively illustrates the equatorward propagation of storm-induced high-latitude disturbances.

Furthermore, during the recovery phase on September 28, the daytime mid-latitude ionosphere showed a considerable negative storm with the TEC being reduced 5–10 TECU as shown in Figure 9b. Meanwhile, the storm-time modification of thermospheric composition also led to a 20%–40% decrease of the O/N_2 ratio in the mid-latitude and a slight increase of ~5%–10% in the low latitudes. Theoretically, Fuller-Rowell et al. (1994) suggested that the storm-time upwelling process should push N_2-rich air upward at mid/high latitudes while pushing O-rich air downward at equatorial/low latitudes. Thus, the F-region O/N_2 on

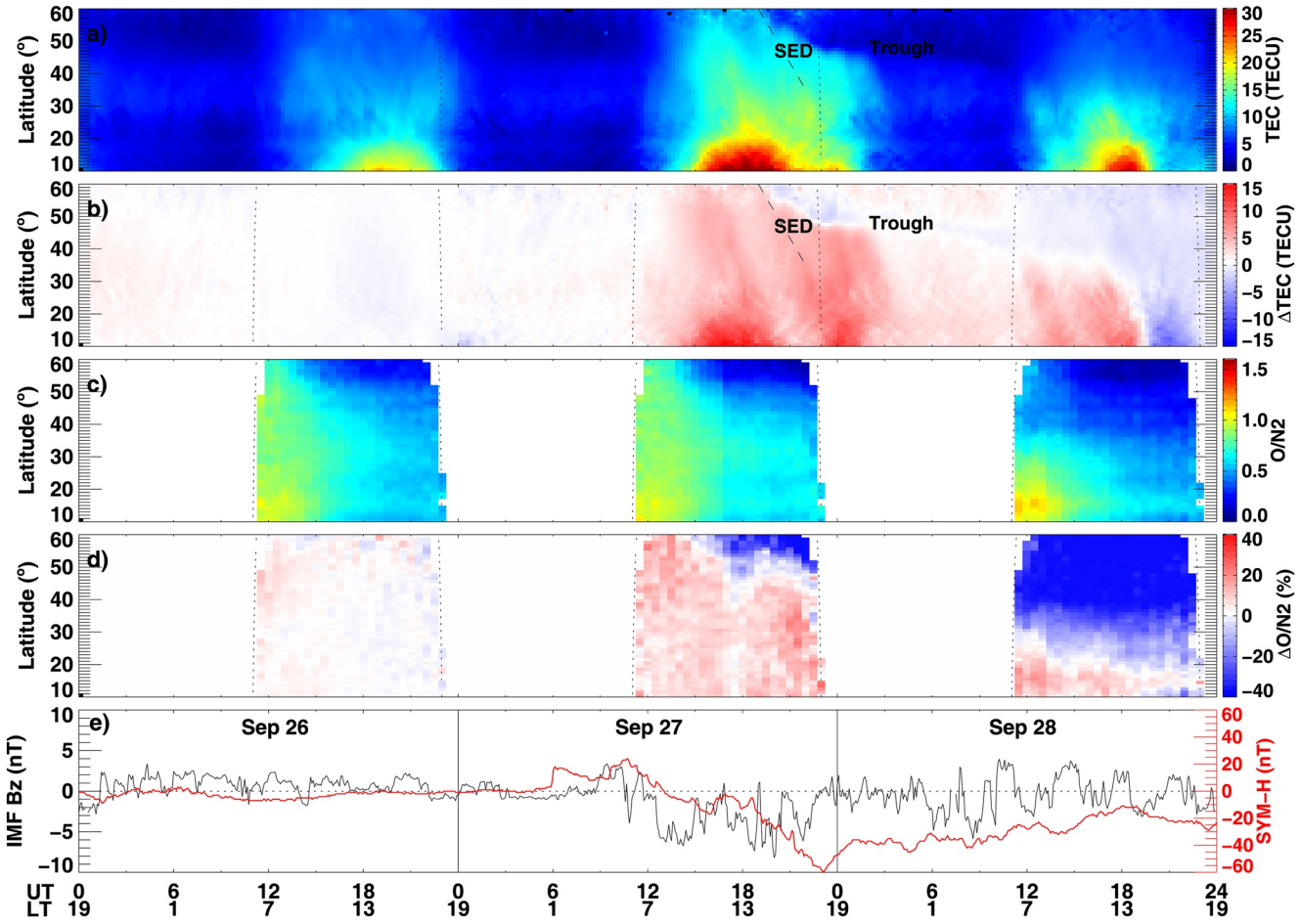

Figure 9. Keogram variations of (a) absolute total electron content (TEC), (b) ΔTEC, (c) O/N_2, and (d) $\Delta O/N_2$ as a function of geographic latitude and universal time in the North American sector that centered at 75°W within ±10° in longitude during September 26–28, 2019. Dotted lines mark the local sunrise and sunset terminators. The storm-enhanced density feature is marked by slant dashed lines, and the storm-time deepened main trough structure is also labeled. (e) Temporal variation of interplanetary magnetic field Bz (black) and symmetric H-component index (red), respectively.

a constant pressure surface would tend to exhibit a reduction at mid/high latitudes and an enhancement at lower latitudes, especially during the storm recovery phase (Prölss, 2008). This mechanism is quite relevant, especially considering GOLD observations are inherently equivalent to constant pressure surface observations (Eastes et al., 2020). As shown in our results, this composition alteration at mid-latitudes tends to increase the ion loss rate and cause the negative ionospheric storm therein (Cai et al., 2020, 2021; Crowley et al., 2006; Prölss, 1976). Moreover, this negative ionospheric storm expanded into the low-latitude region in the local afternoon period after 20 UT (15 LT), leading to the suppression of EIA crest densities of ~10 TECU amplitudes in the Northern Hemisphere. In addition, besides the above-mentioned composition effect, the disturbed thermospheric wind could also build up a disturbance dynamo electric field with a westward direction in the daytime, which would suppress the quiet-time dynamo pattern and form a large contribution to negative ionospheric storm effects in the low latitudes (Blanc & Richmond, 1980; Kuai et al., 2016).

5. Discussion

5.1. SAPS-Related Thermospheric Poleward Wind Surge

The Millstone Hill FPI and ISR measurements in this study demonstrate a striking phenomenon resulting from the effects of SAPS on ionosphere and thermosphere: a strong poleward wind surge of ~85 m/s following an intense westward zonal wind of ~230 m/s was observed in the post-SAPS period. This phenomenon

could be explained by a causal chain of subauroral ion-neutral coupling processes and relevant thermosphere dynamics as follows: (a) Intense westward wind: Recall from Figure 2 that a significant SAPS associated maximum westward ion drift of ~1,000 m/s occurred around 22–24 UT on September 27 in the vicinity of Millstone Hill. In response, neutrals were subject to strong ion drag effects in the SAPS channel via ion-neutral friction and would subsequently form large westward winds, as have been observed and modeled in several prior studies (e.g., Ferdousi et al., 2019; Wang et al., 2011, 2012, 2018; Zhang et al., 2015). Due to the time scales of these effects, there was a 2–3 h time delay between the westward neutral wind disturbance and SAPS flow both for their initiation and peak responses. (b) Strong poleward wind surge: Besides our result, a similar SAPS event with poleward wind surge was observed by Zhang et al. (2015) and simulated by Guo et al. (2018) for the 2015 St. Patrick's day storm. Both studies indicated that the Coriolis force on the westward zonal wind contributed to its northward rotating and subsequent poleward surge. Moreover, Guo et al. (2018) suggested that the pressure gradient due to storm-time TAD/TID related to auroral and frictional heating could play a dominant role in triggering such a poleward wind surge. Shiokawa et al. (2003) also observed poleward wind enhancement at mid-latitudes during a major storm event and indicated that it correlated with LSTIDs. Recall from Figure 4 that both significant auroral-induced TIDs as well as subauroral TID feature with divergent propagation components were observed during the storm main phase before the appearance of poleward wind. The simulation in Zhang et al. (2015) indicated the Coriolis forcing was able to establish the poleward wind in 1–2 h, consistent with both the observed time lag from a zonal wind enhancement to poleward wind evolution and with the observed poleward wind peak velocity. However, this fundamental forcing resulted in only a smooth and gradual increase in the poleward wind. In the end, therefore, TADs/TIDs originated either by auroral or subauroral processes can provide a swift poleward wind surge but would need to meet specific excitation and propagation conditions to match the observed timing of the wind surge.

5.2. SAPS-Induced TIDs

Coincident occurrence of westward propagating TIDs and strong SAPS was found in the North American subauroral region near Millstone Hill ISR. This phenomenon is similar to that reported in Zhang et al. (2019), and the generation mechanisms of these TIDs and their connection with SAPS might be explained as follows: (a) Gravity waves due to SAPS-induced frictional heating: It is known that SAPS will cause significant frictional heating due to large ion-neutral relative velocity therein (Anderson et al., 1991; Rodger, 2008). Guo et al. (2018) indicated that the intense frictional heating effect due to SAPS could cause neutral temperature and composition changes, resulting in acoustic-gravity waves that propagate away in the form of TAD/TIDs near the SAPS region. (b) Amplification of the Perkins instability growth rate due to SAPS electric field: Besides gravity waves, electrodynamic forces under a favorable condition of the Perkins instability (Perkins, 1973) could also explain the formation of mid-latitude medium-scale TIDs, though Perkins instability growth rates are usually quite small (Kelley & Fukao, 1991). Zhang et al. (2019) indicated that a strong magnetically poleward SAPS electric field could effectively amplify the Perkins instability growth rate, so that TIDs with a strong polarization electric field variation can be generated in the subauroral region. A future theoretical study is needed to further address the mechanism.

5.3. Interplay Between SAPS and SED

A notable SED feature associated with dusktime positive ionospheric storm conditions can be seen in Figures 9a and 9b as a plume-like large-amplitude TEC structure marked by dashed lines. This SED feature was also observed by the Millstone Hill incoherent scatter radar as shown in Figure 5. SED occurrence during such a minor but geo-effective storm is quite interesting, and it can potentially be ascribed to a combination of the following mechanisms: (a) Zonal ion transport driven by SAPS or enhanced convection flow: The poleward edge of SED is collocated with the equatorward wall of the deepened main trough where intense SAPS flow existed as shown in Figure 2. Moreover, Figure 9b shows that the storm-time main trough feature was much more pronounced than the previous quiet day. This indicates the presence of SAPS, since the enhanced ion temperature within SAPS could accelerate the recombination rate therein (Aa, Zou, et al., 2020; Rodger, 2008). Under these factors, plume materials could be effectively carried sunward from the nightside to the dayside in the SAPS overlapping region (Foster et al., 2007). Figures 9a and 9b also showed that the

main trough channel was significantly deepened and pushed equatorward around dusktime, indicating the equatorward expansion of the convection pattern. Foster (1993) suggested that the expansion of high-latitude convection in the afternoon sector can pick up high-density plasma on its equatorward edge and transport it toward the cusp. (b) Ion transport across wide latitudinal regions: Some prior studies indicated that the peak of equatorial ionization anomaly could be pushed toward higher latitudes due to enhanced fountain effect though this effect is most likely a severe storm feature (e.g., Gardner et al., 2018; Kelley et al., 2004; Tsurutani et al., 2004). In our results, Figure 8b show synchronous mid-latitude and low-latitude TEC enhancement of ∼10 TECU around the dusk sector. It is likely therefore that the TEC enhancement within the SED extended from the EIA crest region to higher latitudes, providing a seed population for density increases to be carried by SAPS and/or convection flow.

6. Conclusions

In this study, we have investigated SAPS-related ion-neutral coupling processes and related mid-latitude ionosphere and thermosphere responses during a modest but geo-effective storm on September 27–28, 2019 around the recent deep solar minimum. The effects of SAPS on midlatitude electrodynamics and dynamics in the North American sector were comprehensively analyzed using Millstone Hill incoherent scatter radar data, FPI measurements, GNSS TEC, DMSP cross-track drifts, and PFISR measurements, as well as GOLD O/N_2 data. A number of salient and interesting features of ionospheric/thermospheric disturbances during the storm were recognized and summarized as follows:

1. Both ground-based incoherent scatter radar and DMSP cross-track measurements showed evidence of strong SAPS flow of 1,000 m/s in the North American sector during 20–24 UT on September 27. Deepened main trough structure associated with SAPS was observed in GNSS TEC data, likely due to enhanced frictional heating and ion loss caused by SAPS. Considerable ion upflow of ∼50 m/s in the F region was also measured at Millstone Hill during a SAPS-influenced interval in the local afternoon.
2. Around two hours after SAPS peak flow, a westward neutral wind peak of 230 m/s was observed by the FPI at Millstone Hill during 00–01 UT on September 28, driven by SAPS-related accumulative ion-drag effects. Later, the meridional wind showed a drastic turning from −170 m/s (equatorward) at 0030 UT to 85 m/s (poleward) at 0230 UT. This unusual poleward wind surge was possibly caused by the combining effects of the Coriolis force on the enhanced westward neutral wind and pressure gradients due to storm-time TAD/TIDs. The neutral drag effect of this poleward wind surge also caused concurrent large downward ion flow of 50–100 m/s at Millstone Hill.
3. During the storm main phase, intense daytime LSTIDs were generated in the auroral zone and propagated equatorward in the North American sector with a wavelength of 2,000–2,500 km and periods of 40–50 min. However, the occurrence of dusktime SAPS caused significant changes to TID propagation and excitation. Under the influence of SAPS frictional heating and electric field, the previous zonal wavefronts started to rotate and break, exhibiting prominent divergent patterns with additional westward propagating TID components.
4. A significant SED feature was collectively observed by (a) GNSS TEC as an enhanced TEC structure and (b) Millstone Hill ISR as an enhanced *Ne* band with upward ion drift of 50 m/s in the local afternoon sector. In addition, the main trough and SAPS were simultaneously observed near the poleward edge of SED, and SED was also observed by PFISR associated with northwestward plasma flows. These facts suggest that a combination of zonal ion transport driven by strong westward plasma flow and $\mathbf{E} \times \mathbf{B}$ plasma drift projected in the vertical direction, with some contribution from ion transportation across latitudes, collectively generated this considerable storm-time SED feature.
5. A prolonged positive ionospheric and thermospheric storm feature occurred at mid-latitudes for more than 12 h during the main phase and early part of the recovery phase, with TEC enhancement of ∼5–10 TECU and column O/N_2 ratio increase of ∼10%–20%. This positive I-T storm effect could be collectively generated by atomic oxygen downwelling caused by storm-time thermospheric circulation, combined with plasma uplifting due to the equatorward neutral wind and enhanced storm-time TAD/TIDs.
6. A synchronous negative storm effect across the mid-latitude ionosphere and thermosphere was observed during the later half of the recovery phase, with TEC reduction of ∼5–10 TECU and column O/N_2 ratio decrease of ∼20%–40%. This phenomenon could be largely caused by thermospheric composition change, plus some contribution from disturbance dynamo electric field.

In aggregate, the presence of these substantial, and perhaps unexpected, ionosphere and thermosphere effects during a deep solar minimum, modest strength geomagnetic storm provide compelling evidence of the significant role of magnetosphere-ionosphere-thermosphere coupling in upper atmosphere dynamics. Future modeling and observational studies are encouraged to further explore the range of ionospheric and thermospheric variability such coupling can provide under an expanded range of solar and geomagnetic conditions.

Data Availability Statement

Millstone Hill incoherent scatter radar observation and GNSS TEC data products are provided to the community through the Madrigal distributed data system at (http://cedar.openmadrigal.org/) by the Massachusetts Institute of Technology (MIT) under NSF grant AGS-1952737. The PFISR data are available at the SRI AMISR database (https://data.amisr.com/database/61/) and the Madrigal CEDAR database (http://cedar.openmadrigal.org/). The FPI data are available at the Madrigal CEDAR database (http://cedar.openmadrigal.org/). The DMSP SSIES data are available at NOAA NGDC (satdat.ngdc.noaa.gov/dmsp/) and the Madrigal CEDAR database (http://cedar.openmadrigal.org/). The GOLD data are provided to the public by NASA/GOLD mission science team (https://gold.cs.ucf.edu/). The solar and geophysical parameters data is acquired from NASA/GSFC's Space Physics Data Facility's OMNIWeb service (https://cdaweb.gsfc.nasa.gov/) and Kyoto world data center for Geomagnetism (http://wdc.kugi.kyoto-u.ac.jp/).

Acknowledgments
Millstone Hill incoherent scatter radar observation and GNSS TEC data are part of the U.S. NSF Geospace Facility program under a cooperative agreement AGS-1952737 with Massachusetts Institute of Technology, which also supported in part research activity by MIT Haystack Observatory members. S. R. Zhang and A. J. Coster acknowledge the AFOSR support for the MURI Project FA9559-16-1-0364; and A. J. Coster, S. R. Zhang and L. P. Goncharenko acknowledge the ONR Grant N00014-17-1-2186. Data for the TEC processing is provided from the following organizations: The Crustal Dynamics Data Information System (CDDIS), the Scripps Orbit and Permanent Array Center (SOPAC), the Continuously Operating Reference System (CORS), the EUREF Permanent GNSS network (EPN), the University NAVSTAR Consortium (UNAVCO), Institut Geographique National in France (IGN), the Brazilian Network for Continuous Monitoring (RBMC), National Geodetic Survey, Instituto Brasileiro de Geografia e Estatstica, RAMSAC CORS of Instituto Geogrfico Nacional de la Repblica Argentina, Arecibo Observatory, Low-Latitude Ionospheric Sensor Network (LISN), Topcon Positioning Systems, Inc., Canadian High Arctic Ionospheric Network, Centro di Ricerche Sismologiche, Systme d'Observation du Niveau des Eaux Littorales (SONEL), RENAG: REseau NAtional GPS permanent, GeoNet - the official source of geological hazard information for New Zealand, GNSS Reference Networks, Finnish Meteorological Institute, SWEPOS—Sweden.

References

Aa, E., Erickson, P. J., Zhang, S.-R., Zou, S., Coster, A. J., Goncharenko, L. P., & Foster, J. C. (2020). A statistical study of the subauroral polarization stream over North American sector using the millstone Hill incoherent scatter radar 1979-2019 measurements. *Journal of Geophysical Research: Space Physics*, *125*(10), e28584. https://doi.org/10.1029/2020JA028584

Aa, E., Zou, S., Erickson, P. J., Zhang, S.-R., & Liu, S. (2020). Statistical analysis of the main ionospheric trough using Swarm in situ measurements. *Journal of Geophysical Research: Space Physics*, *125*(3), e27583. https://doi.org/10.1029/2019JA027583

Aa, E., Zou, S., Ridley, A., Zhang, S., Coster, A. J., Erickson, P. J., et al. (2019). Merging of storm time midlatitude traveling ionospheric disturbances and equatorial plasma bubbles. *Space Weather*, *17*(2), 285–298. https://doi.org/10.1029/2018SW002101

Anderson, P. C., Heelis, R. A., & Hanson, W. B. (1991). The ionospheric signatures of rapid subauroral ion drifts. *Journal of Geophysical Research*, *96*(A4), 5785–5792. https://doi.org/10.1029/90JA02651

Astafyeva, E., Bagiya, M. S., Förster, M., & Nishitani, N. (2020). Unprecedented hemispheric asymmetries during a surprise ionospheric storm: A game of drivers. *Journal of Geophysical Research: Space Physics*, *125*(3), e27261. https://doi.org/10.1029/2019JA027261

Astafyeva, E., Zakharenkova, I., & Förster, M. (2015). Ionospheric response to the 2015 St. Patrick's Day storm: A global multi-instrumental overview. *Journal of Geophysical Research: Space Physics*, *120*(10), 9023–9037. https://doi.org/10.1002/2015JA021629

Astafyeva, E., Zakharenkova, I., Huba, J. D., Doornbos, E., & van den IJssel, J. (2017). Global ionospheric and thermospheric effects of the June 2015 geomagnetic disturbances: Multi-instrumental observations and modeling. *Journal of Geophysical Research: Space Physics*, *122*(11), 11742. https://doi.org/10.1002/2017JA024174

Balan, N., Shiokawa, K., Otsuka, Y., Kikuchi, T., Vijaya Lekshmi, D., Kawamura, S., & Bailey, G. J. (2010). A physical mechanism of positive ionospheric storms at low latitudes and midlatitudes. *Journal of Geophysical Research*, *115*(A2), A02304. https://doi.org/10.1029/2009JA014515

Blanc, M., & Richmond, A. D. (1980). The ionospheric disturbance dynamo. *Journal of Geophysical Research*, *85*(A4), 1669–1686. https://doi.org/10.1029/JA085iA04p01669

Buonsanto, M. J. (1999). Ionospheric storms—A review. *Space Science Review*, *88*, 563–601. https://doi.org/10.1023/A:1005107532631

Buonsanto, M. J., Foster, J. C., & Sipler, D. P. (1992). Observations from millstone hill during the geomagnetic disturbances of March and April 1990. *Journal of Geophysical Research*, *97*(A2), 1225–1243. https://doi.org/10.1029/91JA02428

Burns, A. G., Killeen, T. L., Deng, W., Carignan, G. R., & Roble, R. G. (1995). Geomagnetic storm effects in the low- to middle-latitude upper thermosphere. *Journal of Geophysical Research*, *100*(A8), 14673–14692. https://doi.org/10.1029/94JA03232

Burns, A. G., Killeen, T. L., & Roble, R. G. (1991). A theoretical study of thermospheric composition perturbations during a impulsive geomagnetic storm. *Journal of Geophysical Research*, *96*(A8), 14153–14167. https://doi.org/10.1029/91JA00678

Cai, X., Burns, A. G., Wang, W., Qian, L., Pedatella, N., Coster, A., et al. (2021). Variations in thermosphere composition and ionosphere total electron content under 'geomagnetically quiet' conditions at solar-minimum. *Geophysical Research Letters*, *48*(11). https://doi.org/10.1029/2021gl093300

Cai, X., Burns, A. G., Wang, W., Qian, L., Solomon, S. C., Eastes, R. W., et al. (2020). The two-dimensional evolution of thermospheric $\sum O/N^2$ response to weak geomagnetic activity during solar-minimum observed by GOLD. *Geophysical Research Letters*, *47*(18). https://doi.org/10.1029/2020gl088838

Coster, A. J., & Foster, J. (2007). Space-weather impacts of the sub-auroral polarization stream. *URSI Radio Science Bulletin*, *2007*(321), 28–36.

Crowley, G., Hackert, C. L., Meier, R. R., Strickland, D. J., Paxton, L. J., Pi, X., & Wene, G. (2006). Global thermosphere-ionosphere response to onset of 20 November 2003 magnetic storm. *Journal of Geophysical Research*, *111*(A10), A10S18. https://doi.org/10.1029/2005JA011518

Crowley, G., & Meier, R. R. (2008). Disturbed O/N_2 ratios and their transport to middle and low latitudes. In P. M. Kintner, A. J. Coster, T. Fuller-Rowell, A. J. Mannucci, M. Mendillo, & R. Heelis (Eds.), *Midlatitude ionospheric dynamics and disturbances, Geophysical Monograph Series* (Vol. 181, pp. 221–234). Washington, DC: American Geophysical Union. https://doi.org/10.1029/181GM20

Deng, W., Killeen, T. L., Burns, A. G., Roble, R. G., Slavin, J. A., & Wharton, L. E. (1993). The effects of neutral inertia on ionospheric currents in the high-latitude thermosphere following a geomagnetic storm. *Journal of Geophysical Research*, *98*(A5), 7775–7790. https://doi.org/10.1029/92JA02268

Ding, F., Wan, W., Ning, B., & Wang, M. (2007). Large-scale traveling ionospheric disturbances observed by GPS total electron content during the magnetic storm of 29–30 October 2003. *Journal of Geophysical Research*, *112*(A6), A06309. https://doi.org/10.1029/2006JA012013

Doherty, P., Coster, A. J., & Murtagh, W. (2004). Space weather effects of October–November 2003. *GPS Solutions*, *8*, 267–271. https://doi.org/10.1007/s10291-004-0109-3

Eastes, R. W., McClintock, W. E., Burns, A. G., Anderson, D. N., Andersson, L., Aryal, S., & Woods, T. N. (2020). Initial observations by the GOLD mission. *Journal of Geophysical Research: Space Physics*, *125*(7), e27823. https://doi.org/10.1029/2020JA027823

Eastes, R. W., Solomon, S. C., Daniell, R. E., Anderson, D. N., Burns, A. G., England, S. L., & McClintock, W. E. (2019). Global-scale observations of the equatorial ionization anomaly. *Geophysical Research Letters*, *46*(16), 9318–9326. https://doi.org/10.1029/2019GL084199

Erickson, P., Goncharenko, L., Nicolls, M., Ruohoniemi, M., & Kelley, M. (2010). Dynamics of North American sector ionospheric and thermospheric response during the November 2004 superstorm. *Journal of Atmospheric and Solar-Terrestrial Physics*, *72*(4), 292–301. https://doi.org/10.1016/j.jastp.2009.04.001

Erickson, P. J., Beroz, F., & Miskin, M. Z. (2011). Statistical characterization of the American sector subauroral polarization stream using incoherent scatter radar. *Journal of Geophysical Research*, *116*, A00J21. https://doi.org/10.1029/2010JA015738

Evans, J. V. (1969). Theory and practice of ionosphere study by Thomson scatter radar. *Proceedings of the IEEE*, *57*(4), 496–530. https://doi.org/10.1109/PROC.1969.7005

Ferdousi, B., Nishimura, Y., Maruyama, N., & Lyons, L. R. (2019). Subauroral neutral wind driving and its feedback to SAPS during the 17 March 2013 geomagnetic storm. *Journal of Geophysical Research: Space Physics*, *124*(3), 2323–2337. https://doi.org/10.1029/2018JA026193

Foster, J. C. (1993). Storm time plasma transport at middle and high latitudes. *Journal of Geophysical Research*, *98*(A2), 1675–1690. https://doi.org/10.1029/92JA02032

Foster, J. C., & Burke, W. J. (2002). SAPS: A new categorization for sub-auroral electric fields. *EOS Transactions*, *83*(36), 393. https://doi.org/10.1029/2002EO000289

Foster, J. C., Coster, A. J., Erickson, P. J., Holt, J. M., Lind, F. D., Rideout, W., & Rich, F. J. (2005). Multiradar observations of the polar tongue of ionization. *Journal of Geophysical Research*, *110*(A9), A09S31. https://doi.org/10.1029/2004JA010928

Foster, J. C., Rideout, W., Sandel, B., Forrester, W. T., & Rich, F. J. (2007). On the relationship of SAPS to storm-enhanced density. *Journal of Atmospheric and Solar-Terrestrial Physics*, *69*(3), 303–313. https://doi.org/10.1016/j.jastp.2006.07.021

Foster, J. C., & Vo, H. B. (2002). Average characteristics and activity dependence of the subauroral polarization stream. *Journal of Geophysical Research*, *107*(A12), 1475. https://doi.org/10.1029/2002JA009409

Fuller-Rowell, T. J., Codrescu, M. V., Moffett, R. J., & Quegan, S. (1994). Response of the thermosphere and ionosphere to geomagnetic storms. *Journal of Geophysical Research*, *99*(A3), 3893–3914. https://doi.org/10.1029/93JA02015

Galperin, Y., Ponomarov, Y., & Zosinova, A. (1974). Plasma convection in polar ionosphere. *Annales de Geophysique*, *30*(1–7).

Gardner, L. C., Schunk, R. W., Scherliess, L., Eccles, V., Basu, S., & Valladeres, C. (2018). Modeling the midlatitude ionosphere storm-enhanced density distribution with a data assimilation model. *Space Weather*, *16*(10), 1539–1548. https://doi.org/10.1029/2018SW001882

Goncharenko, L. P., Harvey, V. L., Greer, K. R., Zhang, S. R., & Coster, A. J. (2020). Longitudinally dependent low-latitude ionospheric disturbances linked to the antarctic sudden stratospheric warming of September 2019. *Journal of Geophysical Research: Space Physics*, *125*(8), e28199. https://doi.org/10.1029/2020JA028199

Guo, J.-P., Deng, Y., Zhang, D.-H., Lu, Y., Sheng, C., & Zhang, S.-R. (2018). The effect of subauroral polarization streams on ionosphere and thermosphere during the 2015 St. Patrick's Day storm: Global ionosphere-thermosphere model simulations. *Journal of Geophysical Research*, *123*(3), 2241–2256. https://doi.org/10.1002/2017JA024781

Hairston, M., Coley, W. R., & Stoneback, R. (2016). Responses in the polar and equatorial ionosphere to the March 2015 St. Patrick Day storm. *Journal of Geophysical Research: Space Physics*, *121*(11), 11234. https://doi.org/10.1002/2016JA023165

Huang, C.-S., Rich, F. J., & Burke, W. J. (2010). Storm time electric fields in the equatorial ionosphere observed near the dusk meridian. *Journal of Geophysical Research*, *115*(A8), A08313. https://doi.org/10.1029/2009JA015150

Huang, C.-S., Wilson, G. R., Hairston, M. R., Zhang, Y., Wang, W., & Liu, J. (2016). Equatorial ionospheric plasma drifts and o+ concentration enhancements associated with disturbance dynamo during the 2015 st. patrick's day magnetic storm. *Journal of Geophysical Research: Space Physics*, *121*(8), 7961–7973. https://doi.org/10.1002/2016JA023072

Huba, J. D., Sazykin, S., & Coster, A. (2017). SAMI3-RCM simulation of the 17 March 2015 geomagnetic storm. *Journal of Geophysical Research: Space Physics*, *122*(1), 1246–1257. https://doi.org/10.1002/2016JA023341

Hunsucker, R. D. (1982). Atmospheric gravity waves generated in the high-latitude ionosphere: A review. *Reviews of Geophysics and Space Physics*, *20*, 293. https://doi.org/10.1029/RG020i002p00293

Immel, T. J., Crowley, G., Craven, J. D., & Roble, R. G. (2001). Dayside enhancements of thermospheric O/N_2 following magnetic storm onset. *Journal of Geophysical Research*, *106*(A8), 15471–15488. https://doi.org/10.1029/2000JA000096

Jimoh, O., Lei, J., Zhong, J., Owolabi, C., Luan, X., & Dou, X. (2019). Topside ionospheric conditions during the 7–8 September 2017 geomagnetic storm. *Journal of Geophysical Research: Space Physics*, *124*(11), 9381–9404. https://doi.org/10.1029/2019JA026590

Jonah, O. F., Coster, A., Zhang, S., Goncharenko, L., Erickson, P. J., de Paula, E. R., & Kherani, E. A. (2018). TID observations and source analysis during the 2017 memorial day weekend geomagnetic storm over North America. *Journal of Geophysical Research: Space Physics*, *123*(10), 8749–8765. https://doi.org/10.1029/2018JA025367

Kelley, M. C., & Fukao, S. (1991). Turbulent upwelling of the mid-latitude ionosphere 2. Theoretical framework. *Journal of Geophysical Research*, *96*(A3), 3747–3753. https://doi.org/10.1029/90JA02252

Kelley, M. C., Vlasov, M. N., Foster, J. C., & Coster, A. J. (2004). A quantitative explanation for the phenomenon known as storm-enhanced density. *Geophysical Research Letters*, *31*(19), L19809. https://doi.org/10.1029/2004GL020875

Kikuchi, T., Araki, T., Maeda, H., & Maekawa, K. (1978). Transmission of polar electric fields to the equator. *Nature*, *273*, 650. https://doi.org/10.1038/273650a0

Killeen, T. L., & Roble, R. G. (1984). An analysis of the high-latitude thermospheric wind pattern calculatd by a Thermospheric general circulation model 1. Momentum forcing. *Journal of Geophysical Research*, *89*(A9), 7509–7522. https://doi.org/10.1029/JA089iA09p07509

Klimenko, M. V., & Klimenko, V. V. (2012). Disturbance dynamo, prompt penetration electric field and overshielding in the Earth's ionosphere during geomagnetic storm. *Journal of Atmospheric and Solar-Terrestrial Physics*, *90*, 146–155. https://doi.org/10.1016/j.jastp.2012.02.018

Kuai, J., Liu, L., Liu, J., Sripathi, S., Zhao, B., Chen, Y., & Hu, L. (2016). Effects of disturbed electric fields in the low-latitude and equatorial ionosphere during the 2015 St. Patrick's day storm. *Journal of Geophysical Research: Space Physics*, *121*(9), 9111–9126. https://doi.org/10.1002/2016JA022832

Lei, J., Huang, F., Chen, X., Zhong, J., Ren, D., Wang, W., & Xue, X. (2018). Was magnetic storm the only driver of the long-duration enhancements of daytime total electron content in the Asian-Australian sector between 7 and 12 September 2017? *Journal of Geophysical Research: Space Physics*, *123*(4), 3217–3232. https://doi.org/10.1029/2017JA025166

Liu, L., Zou, S., Yao, Y., & Aa, E. (2019). Multi-scale ionosphere responses to the May 2017 magnetic storm over the Asian sector. *GPS Solutions*, *24*, 1–15. https://doi.org/10.1007/s10291-019-0940-1

Lu, G., Goncharenko, L., Nicolls, M. J., Maute, A., Coster, A., & Paxton, L. J. (2012). Ionospheric and thermospheric variations associated with prompt penetration electric fields. *Journal of Geophysical Research*, *117*(A8), A08312. https://doi.org/10.1029/2012JA017769

Lu, G., Goncharenko, L. P., Richmond, A. D., Roble, R. G., & Aponte, N. (2008). A dayside ionospheric positive storm phase driven by neutral winds. *Journal of Geophysical Research*, *113*(A8), A08304. https://doi.org/10.1029/2007JA012895

Lu, G., Hagan, M. E., Häusler, K., Doornbos, E., Bruinsma, S., Anderson, B. J., & Korth, H. (2014). Global ionospheric and thermospheric response to the 5 April 2010 geomagnetic storm: An integrated data-model investigation. *Journal of Geophysical Research: Space Physics*, *119*(12), 10375. https://doi.org/10.1002/2014JA020555

Lyons, L. R., Killeen, T. L., & Walterscheid, R. L. (1985). The neutral wind "flywheel" as a source of quiet-time, polar-cap currents. *Geophysical Research Letters*, *12*(2), 101–104. https://doi.org/10.1029/GL012i002p00101

Lyons, L. R., Nishimura, Y., Gallardo-Lacourt, B., Nicolls, M. J., Chen, S., Hampton, D. L., & Angelopoulos, V. (2015). Azimuthal flow bursts in the inner plasma sheet and possible connection with SAPS and plasma sheet earthward flow bursts. *Journal of Geophysical Research: Space Physics*, *120*(6), 5009–5021. https://doi.org/10.1002/2015JA021023

Maruyama, N., Richmond, A. D., Fuller-Rowell, T. J., Codrescu, M. V., Sazykin, S., Toffoletto, F. R., & Millward, G. H. (2005). Interaction between direct penetration and disturbance dynamo electric fields in the storm-time equatorial ionosphere. *Geophysical Research Letters*, *32*(17), L17105. https://doi.org/10.1029/2005GL023763

McClintock, W. E., Eastes, R. W., Beland, S., Bryant, K. B., Burns, A. G., Correira, J., & Veibel, V. (2020). Global-scale observations of the limb and disk mission implementation: 2. Observations, data pipeline, and Level 1 data products. *Journal of Geophysical Research: Space Physics*, *125*(5), e27809. https://doi.org/10.1029/2020JA027809

Mendillo, M. (2006). Storms in the ionosphere: Patterns and processes for total electron content. *Reviews of Geophysics*, *44*(4), RG4001. https://doi.org/10.1029/2005RG000193

Millward, G. H., Moffett, R. J., Balmforth, H. F., & Rodger, A. S. (1999). Modeling the ionospheric effects of ion and electron precipitation in the cusp. *Journal of Geophysical Research*, *104*(A11), 24603–24612. https://doi.org/10.1029/1999JA900249

Nava, B., Rodríguez-Zuluaga, J., Alazo-Cuartas, K., Kashcheyev, A., Migoya-Orué, Y., Radicella, S. M., & Fleury, R. (2016). Middle- and low-latitude ionosphere response to 2015 St. Patrick's Day geomagnetic storm. *Journal of Geophysical Research: Space Physics*, *121*(4), 3421–3438. https://doi.org/10.1002/2015JA022299

Ngwira, C. M., McKinnell, L.-A., Cilliers, P. J., & Coster, A. J. (2012). Ionospheric observations during the geomagnetic storm events on 24–27 July 2004: Long-duration positive storm effects. *Journal of Geophysical Research*, *117*, A00L02. https://doi.org/10.1029/2011JA016990

Perkins, F. (1973). Spread F and ionospheric currents. *Journal of Geophysical Research*, *78*, 218–226. https://doi.org/10.1029/JA078i001p00218

Prölss, G. W. (1976). On explaining the negative phase of ionospheric storms. *Planetary and Space Science*, *24*(6), 607–609. https://doi.org/10.1016/0032-0633(76)90140-9

Prölss, G. W. (2008). Ionospheric storms at mid-latitude: A short review. In P. M. Kintner, A. J. Coster, T. Fuller-Rowell, A. J. Mannucci, M. Mendillo, & R. Heelis (Eds.), *Midlatitude ionospheric dynamics and disturbances, Geophysical Monograph Series* (Vol. 181, pp. 221–234). Washington, DC: American Geophysical Union. https://doi.org/10.1029/181GM03

Raeder, J., Cramer, W. D., Jensen, J., Fuller-Rowell, T., Maruyama, N., Toffoletto, F., & Vo, H. (2016). Sub-auroral polarization streams: A complex interaction between the magnetosphere, ionosphere, and thermosphere. *Journal of Physics: Conference Series*, *767*, 012021. https://doi.org/10.1088/1742-6596/767/1/012021

Richmond, A. D. (1978). Gravity wave generation, propagation, and dissipation in the thermosphere. *Journal of Geophysical Research*, *83*(A9), 4131–4146. https://doi.org/10.1029/JA083iA09p04131

Richmond, A. D., & Lu, G. (2000). Upper-atmospheric effects of magnetic storms: A brief tutorial. *Journal of Atmospheric and Solar-Terrestrial Physics*, *62*(12), 1115–1127. https://doi.org/10.1016/S1364-6826(00)00094-8

Rideout, W., & Coster, A. (2006). Automated GPS processing for global total electron content data. *GPS Solutions*, *10*(3), 219–228. https://doi.org/10.1007/s10291-006-0029-5

Rishbeth, H. (1979). Ion-drag effects in the thermosphere. *Journal of Atmospheric and Terrestrial Physics*, *41*, 885–894. https://doi.org/10.1016/0021-9169(79)90130-2

Rishbeth, H. (1998). How the thermospheric circulation affects the ionospheric F2-layer. *Journal of Atmospheric and Solar-Terrestrial Physics*, *60*(14), 1385–1402. https://doi.org/10.1016/S1364-6826(98)00062-5

Rodger, A. (2008). The mid-latitude trough—revisited. In P. M. Kintner, A. J. Coster, T. Fuller-Rowell, A. J. Mannucci, M. Mendillo, & R. Heelis (Eds.), *Midlatitude ionospheric dynamics and disturbances, Geophysical Monograph Series* (Vol. 181, pp. 221–234). Washington, DC: American Geophysical Union. https://doi.org/10.1029/181GM04

Savitzky, A., & Golay, M. J. E. (1964). Smoothing and differentiation of data by simplified least squares procedures. *Analytical Chemistry*, *36*, 1627–1639. https://doi.org/10.1021/ac60214a047

Schunk, R. W. (1975). Transport equations for aeronomy. *Planetary and Space Science*, *23*(3), 437–485. https://doi.org/10.1016/0032-0633(75)90118-X

Schunk, R. W., & Nagy, A. F. (2000). *Ionospheres: Physics, plasma physics, and chemistry*. Cambridge University Press.

Semeter, J., Butler, T., Heinselman, C., Nicolls, M., Kelly, J., & Hampton, D. (2009). Volumetric imaging of the auroral ionosphere: Initial results from PFISR. *Journal of Atmospheric and Solar-Terrestrial Physics*, *71*(6–7), 738–743. https://doi.org/10.1016/j.jastp.2008.08.014

Shiokawa, K., Otsuka, Y., Ogawa, T., Balan, N., Igarashi, K., Ridley, A. J., & Yumoto, K. (2002). A large-scale traveling ionospheric disturbance during the magnetic storm of 15 September 1999. *Journal of Geophysical Research*, *107*(A6), 1088. https://doi.org/10.1029/2001JA000245

Shiokawa, K., Otsuka, Y., Ogawa, T., Kawamura, S., Yamamoto, M., Fukao, S., & Yumoto, K. (2003). Thermospheric wind during a storm-time large-scale traveling ionospheric disturbance. *Journal of Geophysical Research*, *108*(A12), 1423. https://doi.org/10.1029/2003JA010001

Singh, R., & Sripathi, S. (2017). Ionospheric response to 22–23 June 2015 storm as investigated using ground-based ionosondes and GPS receivers over India. *Journal of Geophysical Research: Space Physics*, *122*(11), 11664. https://doi.org/10.1002/2017JA024460

Spiro, R. W., Heelis, R. A., & Hanson, W. B. (1979). Rapid subauroral ion drifts observed by atmosphere explorer C. *Geophysical Research Letters*, *6*(8), 657–660. https://doi.org/10.1029/GL006i008p00657

Su, Y. J., Caton, R. G., Horwitz, J. L., & Richards, P. G. (1999). Systematic modeling of soft-electron precipitation effects on high-latitude F region and topside ionospheric upflows. *Journal of Geophysical Research*, *104*(A1), 153–164. https://doi.org/10.1029/1998JA900068

Tsurutani, B., Mannucci, A., Iijima, B., Abdu, M. A., Sobral, J. H. A., Gonzalez, W., & Vasyliunas, V. M. (2004). Global dayside ionospheric uplift and enhancement associated with interplanetary electric fields. *Journal of Geophysical Research*, *109*(A8), A08302. https://doi.org/10.1029/2003JA010342

Varney, R. H., Nicolls, M. J., Heinselman, C. J., & Kelley, M. C. (2009). Observations of polar mesospheric summer echoes using PFISR during the summer of 2007. *Journal of Atmospheric and Solar-Terrestrial Physics*, *71*(3–4), 470–476. https://doi.org/10.1016/j.jastp.2009.01.002

Vierinen, J., Coster, A. J., Rideout, W. C., Erickson, P. J., & Norberg, J. (2016). Statistical framework for estimating GNSS bias. *Atmospheric Measurement Techniques*, *9*, 1303–1312. https://doi.org/10.5194/amt-9-1303-2016

Wang, H., Lühr, H., HäUsler, K., & Ritter, P. (2011). Effect of subauroral polarization streams on the thermosphere: A statistical study. *Journal of Geophysical Research*, *116*(A3), A03312. https://doi.org/10.1029/2010JA016236

Wang, H., Zhang, K., Zheng, Z., & Ridley, A. J. (2018). The effect of subauroral polarization streams on the mid-latitude thermospheric disturbance neutral winds: A universal time effect. *Annales Geophysicae*, *36*(2), 509–525. https://doi.org/10.5194/angeo-36-509-2018

Wang, W., Talaat, E. R., Burns, A. G., Emery, B., Hsieh, S.-y., Lei, J., & Xu, J. (2012). Thermosphere and ionosphere response to subauroral polarization streams (SAPS): Model simulations. *Journal of Geophysical Research*, *117*(A7), A07301. https://doi.org/10.1029/2012JA017656

Watari, S. (2017). Geomagnetic storms of cycle 24 and their solar sources. *Earth Planets and Space*, *69*(1), 70. https://doi.org/10.1186/s40623-017-0653-z

Yeh, H. C., & Foster, J. C. (1990). Storm tide heavy ion outflow at mid-latitude. *Journal of Geophysical Research*, *95*(A6), 7881–7891. https://doi.org/10.1029/JA095iA06p07881

Yue, X., Wang, W., Lei, J., Burns, A., Zhang, Y., Wan, W., & Schreiner, W. S. (2016). Long-lasting negative ionospheric storm effects in low and middle latitudes during the recovery phase of the 17 March 2013 geomagnetic storm. *Journal of Geophysical Research: Space Physics*, *121*(9), 9234–9249. https://doi.org/10.1002/2016JA022984

Zakharenkova, I., Astafyeva, E., & Cherniak, I. (2016). GPS and GLONASS observations of large-scale traveling ionospheric disturbances during the 2015 St. Patrick's Day storm. *Journal of Geophysical Research: Space Physics*, *121*(12), 12156. https://doi.org/10.1002/2016JA023332

Zhang, S.-R., Erickson, P. J., Coster, A. J., Rideout, W., Vierinen, J., Jonah, O., & Goncharenko, L. P. (2019). Subauroral and polar traveling ionospheric disturbances during the 7–9 September 2017 storms. *Space Weather*, *17*(12), 1748–1764. https://doi.org/10.1029/2019SW002325

Zhang, S.-R., Erickson, P. J., Foster, J. C., Holt, J. M., Coster, A. J., Makela, J. J., & Kerr, R. B. (2015). Thermospheric poleward wind surge at midlatitudes during great storm intervals. *Geophysical Research Letters*, *42*(13), 5132–5140. https://doi.org/10.1002/2015GL064836

Zhang, S.-R., Erickson, P. J., Zhang, Y., Wang, W., Huang, C., Coster, A. J., & Kerr, R. (2017). Observations of ion-neutral coupling associated with strong electrodynamic disturbances during the 2015 St. Patrick's Day storm. *Journal of Geophysical Research: Space Physics*, *122*(1), 1314–1337. https://doi.org/10.1002/2016JA023307

Zhang, S.-R., Zhang, Y., Wang, W., & Verkhoglyadova, O. P. (2017). Geospace system responses to the St. Patrick's Day storms in 2013 and 2015. *Journal of Geophysical Research: Space Physics*, *122*(6), 6901–6906. https://doi.org/10.1002/2017JA024232

Zhong, J., Wang, W., Yue, X., Burns, A. G., Dou, X., & Lei, J. (2016). Long-duration depletion in the topside ionospheric total electron content during the recovery phase of the March 2015 strong storm. *Journal of Geophysical Research: Space Physics*, *121*(5), 4733–4747. https://doi.org/10.1002/2016JA022469

Zou, S., Moldwin, M. B., Ridley, A. J., Nicolls, M. J., Coster, A. J., Thomas, E. G., & Ruohoniemi, J. M. (2014). On the generation/decay of the storm-enhanced density plumes: Role of the convection flow and field-aligned ion flow. *Journal of Geophysical Research: Space Physics*, *119*(10), 8543–8559. https://doi.org/10.1002/2014JA020408

Zou, S., Ridley, A., Jia, X., Boyd, E., Nicolls, M., Coster, A., & Ruohoniemi, J. M. (2017). PFISR observation of intense ion upflow fluxes associated with an SED during the 1 June 2013 geomagnetic storm. *Journal of Geophysical Research: Space Physics*, *122*(2), 2589–2604. https://doi.org/10.1002/2016JA023697

Zou, S., Ridley, A. J., Moldwin, M. B., Nicolls, M. J., Coster, A. J., Thomas, E. G., & Ruohoniemi, J. M. (2013). Multi-instrument observations of SED during 24–25 October 2011 storm: Implications for SED formation processes. *Journal of Geophysical Research: Space Physics*, *118*(12), 7798–7809. https://doi.org/10.1002/2013JA018860